

# Seismic crustal structure beneath Jeju Volcanic Island, South Korea from teleseismic $P$ -receiver functions

Hyunsun Kang,<sup>1</sup> YoungHee Kim<sup>1</sup>, Junkee Rhie,<sup>1</sup> Tae-Seob Kang<sup>1,2</sup> and Marco Brenna<sup>1,3</sup>

<sup>1</sup>School of Earth and Environmental Sciences, Seoul National University, Seoul 08826, Republic of Korea. E-mail: [younghkim@snu.ac.kr](mailto:younghkim@snu.ac.kr)

<sup>2</sup>Division of Earth Environmental System Science, Pukyong National University, Busan 48513, Republic of Korea

<sup>3</sup>Department of Geology, University of Otago, 360 Leith Street, Dunedin 9054, New Zealand

Accepted 2021 May 24. Received 2021 April 21; in original form 2021 January 28

## SUMMARY

Jeju Island is an intraplate volcanic island with enigmatic origins, located on the continental shelf south of the Korean Peninsula. A dense temporary seismic array, operated on Jeju Island from 2013 to 2015, revealed several important constraints on the magma plumbing system of Jeju Island. In this study, we determined the deep crustal seismic structure beneath Jeju Island from the teleseismic  $P$ -to- $S$  converted phases (receiver functions) recorded from 20 temporary and three permanent stations. We removed the contribution of near-surface reverberations in the resulting receiver functions by applying a resonance removal filter. We estimated crustal  $P$ -to- $S$  velocity ratio ( $V_P/V_S$ ) and discontinuity depth to provide teleseismic constraints on the composition and structure. We observed two major seismic discontinuities, which are the upper boundaries of a mid-to-lower crustal low-velocity zone (LVZ) and the Moho transition zone. The depth to the upper boundary of the LVZ is deep in the west and southeast (24–30 km) and shallow in the northeast (8–11 km). The LVZ can be interpreted as an extensively distributed residual magma plumbing system, with magma batches stalled at various levels and at various degrees of crystallization, consistent with the chemical diversity of Jeju magmas. The seismic characteristics of the Moho transition zone vary greatly among regions. The top interface of the Moho transition zone is at a wide range of depth (26–40 km), and is shallow at 26–29 km depths beneath central Jeju, suggesting a complex Moho topography. The presence of mafic cumulates and partially molten mushes may contribute to the observed shallow seismic discontinuity at a depth of 26–29 km. The lack of obvious crustal thickening below the shield volcano, Mt Halla, may be associated with mantle upwelling or presence of mafic underplating and cumulates below Jeju. Spatial variations of crustal  $V_P/V_S$  represent highly heterogeneous crustal composition, resulting from magma differentiation during the evolution of the island.

**Key words:** Body waves; Time-series analysis; Crustal structure; Crustal imaging; Intraplate processes; Asia.

## 1 INTRODUCTION

Jeju Island is an intraplate volcanic island located to the south of the Korean Peninsula (Fig. 1), formed on continental crust by episodic eruptions since ~1.8 Ma. The oval-shaped island (32 km × 75 km) is approximately 600 km from the nearest plate boundary, the Nankai Trough, where the Philippine Sea Plate is subducting beneath the Eurasian Plate (Fig. 1). Mt Halla, the highest point in South Korea (1947 m above sea level), lies in the centre of the island, with more than 300 eruptive centres (scoria cones and tuff rings/cones) distributed on its flanks (Fig. 2a).

Previous petrological and geochemical studies revealed complex variations in geochemical signatures and eruption patterns in Jeju Island (Tatsumi *et al.* 2005; Brenna *et al.* 2010, 2012a, b). Volcanic activity began on the submerged continental shelf and formed dispersed, small-volume (<0.01 km<sup>3</sup>) alkali basaltic tuff cones/rings (Kang 2003; Sohn & Park 2004; Sohn *et al.* 2008; Sohn & Yoon 2010). After emergence, small-scale basaltic monogenetic volcanism continued forming dispersed scoria cones and lava fields associated with the formation of trachytic lava domes in the southwestern part of the island around 700–800 ka (Koh & Park 2010). Beginning ~0.4 Ma, more voluminous (>1.0 km<sup>3</sup>) lava eruptions formed a composite shield (Brenna *et al.* 2012a, b, 2015; Koh *et al.* 2013). The depth and degree of mantle

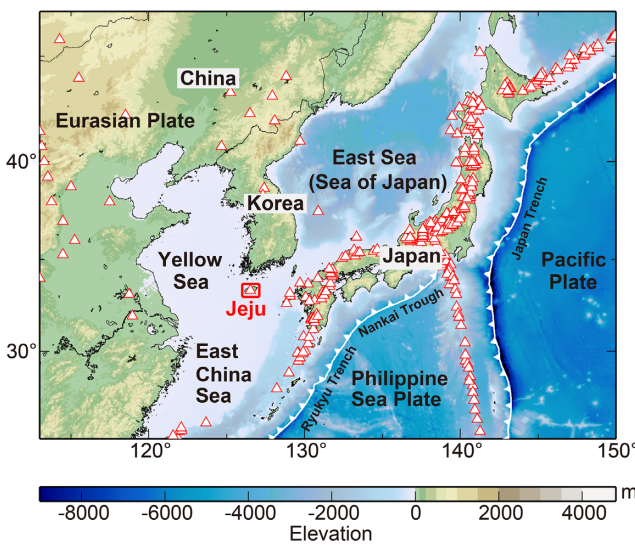


**Figure 1.** A map showing tectonic setting of Jeju Island in northeast Asia. Red box indicates location of Jeju Island. Red outlined triangles indicate locations of Pleistocene–Holocene volcanoes in northeast Asia (Venzke 2013). White saw-toothed lines indicate convergent plate boundaries (Bird 2003).

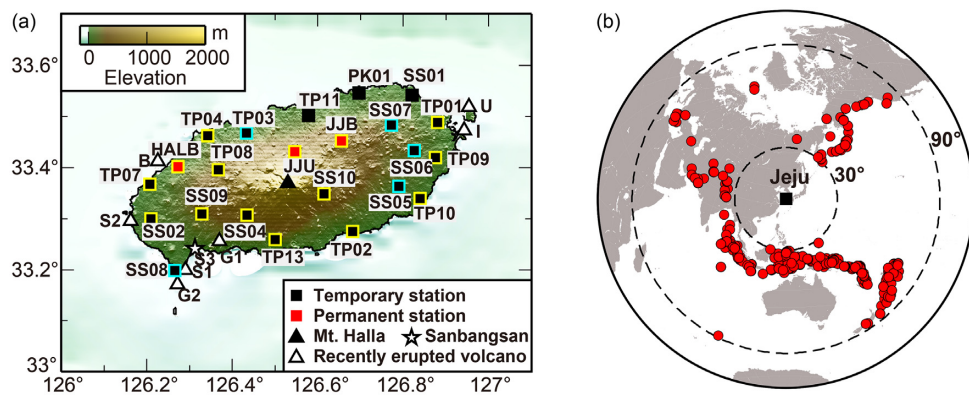


**Figure 2.** Maps showing locations of seismic stations on Jeju Island and distribution of teleseismic earthquakes for teleseismic imaging. (a) A map showing locations of seismic stations. Twenty temporary broad-band stations and three permanent broad-band stations are shown as black and red squares, respectively. Temporary stations were operated during October 2013–November 2015. Two permanent stations (JJU and HALB) belong to the network of the Korea Meteorological Administration (KMA); one permanent station (JJB) belongs to the network of the Korea Institute of Geoscience and Mineral Resources (KIGAM). Note that the resonance removal filter is applied to the RFs of 15 stations (yellow-outlined squares) to correct for the near-surface structure. Cyan-outlined squares indicate the 5 stations yielding low-quality RFs, which are excluded from the  $H\text{-}\kappa$  stacking and CCP stacking analyses. The squares without coloured outlines indicate three stations where no correction for the near-surface structure is applied. Location of central shield volcano, Mt Halla, is shown as a black triangle. Locations of recently erupted ( $< 25$  ka) small-scale volcanoes (B, Biyangdo; S1, Songaksan; S2, Suwolbong; I, Ilchulbong; U, Udo; G1, Gunsan; G2, Gapado; Ahn 2016) are shown as white triangles and denoted by their abbreviations. Location of trachyte volcano, Sanbangsan (S3), is indicated by a white star. (b) Earthquake locations are indicated by red circles. Epicentral distances of  $30^\circ$  and  $90^\circ$  from a central point of the seismic array in Jeju Island (square) are indicated by dashed lines.

partial melting varied over time, thus resulting in diverse chemical composition of magmas, including high-Al alkaline, low-Al alkaline and subalkaline suites (Tatsumi *et al.* 2005; Brenna *et al.* 2012a).

Several models for the formation of Jeju Island have been suggested. Tatsumi *et al.* (2005) proposed that Jeju Island was formed by mantle plume-related magmatism. However, this mechanism is unlikely to explain the volcanic activity of the island due to the lack of typical plume features, such as a volcanic chain with age progression and topographic swells. Shin *et al.* (2012) proposed that Jeju Island was formed by decompression mantle melting due to lithospheric folding under a compressional environment. Brenna *et al.* (2015) suggested that the volcanism in Jeju Island was influenced by distal subduction tectonics at the Kyushu subduction zone, in which enhanced trenchward mantle flow resulting from increased rollback of the Philippine Sea Plate caused mantle upwelling and decompression melting along shear zones. A recent geochemical study by Kim *et al.* (2019) yielded evidence of recycled oceanic crust and sediment components in the mantle source of the Jeju magmas, suggesting that a stagnant subducted Pacific slab in the mantle transition zone may have provided metasomatic fluids to the melting mantle.

There have been few geophysical investigations of Jeju Island; thus far, most have focused on the shallow part of the crust (e.g. volcanic layer and sedimentary cover) using gravity, magnetic, electric, and magnetotelluric data (Lee *et al.* 1983; Lee & Kim 1993; Kwon *et al.* 1995;

Choi *et al.* 2007; Kim & Hong 2012). Several studies using seismic data showed that crustal thickness beneath Jeju ranged from 25 to 35 km (Yoo *et al.* 2007; Jeon *et al.* 2013; Kim *et al.* 2015). However, these estimates of crustal thickness were based on data from five or fewer seismic stations installed on the island, and were therefore limited in their abilities to resolve and interpret overall crustal properties.

In 2013–2015, 20 temporary broad-band stations were deployed on Jeju Island; this constituted the first attempt to operate a dense seismic array on the island, thereby enabling a series of systematic seismic surveys. Using these data, two investigations have been performed to elucidate upper-crustal (1–10 km) velocity structure (Lee *et al.* 2021) and uppermost mantle structure (Song *et al.* 2018). Using teleseismic traveltimes, Song *et al.* (2018) investigated lithospheric structures beneath Jeju Island and identified a deep low-velocity anomaly at a depth of 50–60 km under the summit of Mt Halla, which separates into narrower low-velocity zones at shallower depths (10–45 km). They interpreted the deep and shallow low-velocity anomalies as a high-temperature upper mantle structure with partial melts and a dispersed magmatic system at shallow depth, respectively; thus, they suggested that focused decompression melting at sublithospheric depths may have induced intraplate volcanism in Jeju Island. Furthermore, using ambient noise data, Lee *et al.* (2021) identified seismic anisotropy within the upper crust (1–10 km in depth) beneath Jeju Island; they interpreted this as a layered dike and sill structure, common in the shallow magmatic plumbing of similar volcanic systems (e.g. Keating *et al.* 2008; Kiyosugi *et al.* 2012; Muirhead *et al.* 2016). The present study was performed to use the dense array data to image and better interpret the subsurface crustal structure at the mid-to-lower crustal depth range, thus clarifying relationships with features in the upper crust and uppermost mantle.

In this study, we examined teleseismic  $P$ -to- $S$ -converted phases [or receiver functions (RFs)] to identify the deep crustal structure beneath Jeju Island. We estimated the geometry of crustal discontinuities and  $P$ -to- $S$  velocity ratio ( $V_P/V_S$ ) after correcting for the influence of near-surface layers on the RFs and provided constraints regarding crustal composition and seismic structure. We then migrated the RFs in accordance with the approach proposed by Dueker & Sheehan (1997) to enhance the continuity of the deep seismic structure at the mid-to-lower crustal depth range. In particular, we used the  $V_P/V_S$  estimates to clarify the observed chemical range from basalt to trachyte on Jeju Island (Annen *et al.* 2005; Brenna *et al.* 2012b).

## 2 DATA AND METHODS

### 2.1 Data analysis

We used teleseismic waveform data recorded from the 20 temporary and three permanent broad-band seismic stations deployed on Jeju Island (Fig. 2a). The seismic array covers the whole island (32 km  $\times$  75 km) at average intervals of 9 km. We visually examined all waveforms for earthquakes with magnitudes  $> 5.5$  and within an epicentral distance of 30°–90° from the seismic array, then selected waveforms with a clear  $P$ -wave arrival. In total, 360 earthquakes passed visual quality checks and provided sufficient backazimuthal coverage (Fig. 2b). The number of the earthquakes recorded at 19 stations varied from 23 to 198, and 4 stations had less than 15 earthquakes recorded (Table S1). Notably, the number of selected earthquakes at permanent stations was much greater than the number at temporary stations. We filtered waveforms using a bandpass filter from 0.01 to 1.0 Hz, then cut the waveforms for the time between 10 s before and 60 s after the  $P$ -wave arrival. For the three permanent stations (JJU, JJB and HALB), we corrected misaligned seismograms by applying the orientation angle on the horizontal component seismograms (Lim *et al.* 2018), which are shown in Table S2.

### 2.2 Teleseismic imaging

#### 2.2.1 RF calculation

We computed teleseismic RFs (Langston 1979) to accurately define the location and magnitude of the crustal seismic discontinuities. Given the station array geometry on the island (Fig. 2a), we expected to obtain the highest resolution at the mid-to-lower crustal depths, assuming 25–35 km crust for Jeju Island (Yoo *et al.* 2007; Kim *et al.* 2015, see Fig. S1 for the piercing points of the converted phases).

The RF calculation required two key steps. The first step consisted of coordinate rotation for isolation and separation of incident and scattered wavefields. The second step involved deconvolution, which removed source signature and propagation path effects for each event used in the analysis (Ammon 1991; Rondenay 2009). Following these steps, three orthogonal components of the seismograms (N–E–Z) were rotated to radial–tangential–vertical (R–T–Z) components. R-component seismograms were then deconvolved with Z-component seismograms to generate R-component RFs. We used iterative deconvolution in the time domain (Ligorria & Ammon 1999) with a Gaussian parameter of 2 and a maximum of 100 iterations. Although broad backazimuthal data coverage (Fig. 2b) allowed examination of anisotropic structures from the T-component RFs (hereafter, T-RF) using harmonic decomposition (e.g. Bianchi *et al.* 2010; Kang & Kim 2019), we only focused on imaging the isotropic structure from the R-component RFs (hereafter, R-RF) in this study. We used T-RFs to assess the quality of the obtained R-RFs and excluded R-RFs from further analysis if their corresponding T-RFs showed high amplitude signals at 0–5 s. Based on this criterion, we excluded R-RFs from station SS08 (Fig. 2a). We also note that four stations (TP03, SS05, SS06 and SS07) provided less than 15 R-RFs, and were excluded from further analysis. The five stations that are not used are shown as cyan-outlined squares in Fig. 2(a).

The computed RFs show strong near-surface reverberations, which are typically observed in the presence of low-velocity structures such as thick sediment layers and near-surface volcanics (e.g. Zelt & Ellis 1998; Bannister *et al.*, 2004; Yeck *et al.* 2013; Yu *et al.* 2015; Suhardja

*et al.* 2020). To minimize the resonance caused by complex near-surface low-velocity structures, we applied a resonance removal filter to R-RFs, following a scheme (eq. 1) proposed by Yu *et al.* (2015).

$$F(i\omega) = H(i\omega)(1 + r_0 e^{-i\omega\Delta t}), \quad (1)$$

where  $F(i\omega)$  is the R-RF in the frequency domain after removal of the reverberations,  $H(i\omega)$  is the observed R-RF spectrum and  $(1 + r_0 e^{-i\omega\Delta t})$  is the resonance removal filter. The two parameters  $r_0$  and  $\Delta t$  in the filter represent strength and two-way traveltimes of the reverberations, respectively, which can be determined by autocorrelation of the R-RFs. The two parameters are calculated for each RF trace. Of the 18 stations, 15 stations (Fig. 2a, yellow-outlined squares) showed strong resonance in their RFs (Fig. S2a). We thus applied this filter to those 15 stations and observed that it effectively reduced reverberated phases from the near-surface layer (Fig. S2b).

### 2.2.2 $H-\kappa$ stacking of RFs

We applied  $H-\kappa$  stacking to the RFs to determine depth to crustal discontinuities ( $H$ ) and  $V_p/V_S(\kappa)$ . Stacking RFs from different distances and backazimuths suppress the effects of lateral structural changes and yield an isotropic average crustal velocity model beneath the station, if the backazimuthal and epicentral coverage of events are even and complete (Lim *et al.* 2018). Our RF data set shows generally even distribution of events except for the backazimuthal gap in the east (Fig. 2b), and stacking of the RF data set can lead to an isotropic average crustal velocity below the island.

All reflected or converted modes exhibit a distinct moveout as a function of source-receiver offset. By measuring these moveouts (assuming a locally flat-layered structure), it is possible to estimate local depth and average  $V_p/V_S$  between the surface and the discontinuity associated with each mode (Zhu & Kanamori 2000). In practice, individual modes can be difficult to observe and identify on individual traces; therefore, many events are stacked, and a search is performed over a range of depths to the discontinuity ( $H$ ) and  $V_p/V_S(\kappa)$ . The trade-off between the layer thickness and seismic velocities can be reduced by using both the primary phase ( $Pds$ , where  $d$  represents the subsurface position of a  $P$ -wave impedance contrast) and the later multiples ( $PpPds$  and  $PpSds + PsPds$ ). This method is regarded as conventional  $H-\kappa$  stacking.

In this stacking method, the amplitudes of R-RFs are summed at the predicted arrival times of the converted phase ( $Pds$ ) and its multiples ( $PpPds$  and  $PpSds + PsPds$ ), assuming different  $H$  and  $\kappa$  values. The summation function  $s(H, \kappa)$  is defined as:

$$s(H, \kappa) = w_1r(t_1) + w_2r(t_2) - w_3r(t_3), \quad (2)$$

where  $r(t)$  is the R-RF;  $t_1$ ,  $t_2$  and  $t_3$  are predicted  $Pds$ ,  $PpPds$  and  $PpSds + PsPds$  arrival times at  $H$  and  $\kappa$ , respectively; and  $w_i$  are weighting factors ( $w_1 + w_2 + w_3 = 1$ ; Zhu & Kanamori 2000). The most reliable  $H$  and  $\kappa$  estimates are determined when the three phases are visibly identified and coherently stacked; therefore, maximum amplitude is produced after summation over the grid search range. Uncertainty estimates on the  $H$  and  $\kappa$  are then estimated from the flatness of the summation function at the maximum amplitude in the  $H-\kappa$  domain (Zhu & Kanamori 2000).

We applied this conventional  $H-\kappa$  stacking (Zhu & Kanamori 2000) to the three stations (PK01, SS01 and TP11; Fig. 2a) that showed no or only little reverberations from the near-surface layer (Fig. S2a). We used four sets of unequal weighting factors in the stacking of  $Pds$ ,  $PpPds$  and  $PpSds + PsPds$  phases ( $w_1 = 0.7$ ,  $w_2 = 0.2$ , and  $w_3 = 0.1$ ;  $w_1 = 0.6$ ,  $w_2 = 0.3$ ,  $w_3 = 0.1$ ;  $w_1 = 0.6$ ,  $w_2 = 0.2$ ,  $w_3 = 0.2$ ; and  $w_1 = 0.5$ ,  $w_2 = 0.3$ ,  $w_3 = 0.2$ ). We performed a grid search to find the optimal pair of crustal thickness (in the range of 20–40 km with an interval of 0.1 km) and  $V_p/V_S$  (in the range of 1.5–2 with an interval of 0.0025), assuming  $V_p$  of 6.3 km s<sup>-1</sup>, which is the average value for the crust of the Korean Peninsula (Chang & Baag, 2006, 2007).

For the 15 stations (Fig. 2a, yellow-outlined squares) showing the strong resonance (Fig. S2a), we applied the time-corrected  $H-\kappa$  stacking method of Yu *et al.* (2015) to the RFs that have been corrected for near-surface effects. The method is designed to estimate the subsediment crustal thickness and  $V_p/V_S$  by correcting the delay effects of the sediment layer in the conventional  $H-\kappa$  stacking (Zhu & Kanamori 2000). As we described earlier, the resonance filter (eq. 1) was applied to those 15 stations to reduce the influence of the near-surface structure (Fig. S2b). Using these filtered RFs, the subsediment crustal thickness and  $V_p/V_S$  can be estimated based on the time-corrected  $H-\kappa$  stacking formula:

$$s'(H, \kappa) = w_1r'(t_1 + \delta t) + w_2r'(t_2 + \Delta t - \delta t) - w_3r'(t_3 + \Delta t), \quad (3)$$

where  $r'(t)$  is the filtered R-RF;  $\delta t$  is the time delay of the  $Pbs$  phase ( $Ps$  phase converted at the bottom ( $b$ ) of the sedimentary layer) relative to the direct  $P$ ;  $\Delta t$  is the two-way traveltimes of the reverberations determined from autocorrelation of the RF; and  $w_1$ ,  $w_2$  and  $w_3$  are weighting factors that satisfy  $w_1 + w_2 + w_3 = 1$  (Zhu & Kanamori 2000).  $t_1$ ,  $t_2$  and  $t_3$  are predicted  $Pms$ ,  $PpPms$  and  $PpSms + PsPms$  arrival times at subsediment crustal thickness ( $H$ ) and  $V_p/V_S(\kappa)$ , respectively. The maximum amplitude of  $s'(H, \kappa)$  corresponds to an optimal pairing of  $H$  and  $\kappa$ . The same weighting factors and grid search range for crustal thickness and  $V_p/V_S$  are used as in the conventional  $H-\kappa$  stacking for the three stations.

After the step for the subsediment crustal thickness and  $V_p/V_S$  based on eq. (3), we determine sedimentary thickness and  $V_p/V_S$  for the 15 stations based on a grid search algorithm, following the approach of Yu *et al.* (2015). The grid search is performed using the following equation:

$$A(H, \kappa) = w_4r'(t_4) + w_2r'(t_2) - w_3r'(t_3), \quad (4)$$

where  $H$  and  $\kappa$  indicate a pair of candidate sedimentary thickness (in the range of 0–4 km with an interval of 0.05 km) and  $V_p/V_s$  (in the range of 1.5–5 with an interval of 0.0025).  $w_4$ ,  $w_2$  and  $w_3$  are the weighting factors for  $Pbs$ ,  $PpPms$  and  $PpSms$ , respectively. We used the same weighting factors that Yu *et al.* (2015) used ( $w_4 = 0.05$ ,  $w_2 = 0.7$  and  $w_3 = 0.25$ ). Finally,  $t_4$ ,  $t_2$  and  $t_3$  are the moveout of  $Pbs$ ,  $PpPms$  and  $PpSms$  phases through the sedimentary and subsediment crustal layers, respectively. The  $t_4$ ,  $t_2$  and  $t_3$  can be calculated from the following equations:

$$t_4 = \int_{-H}^0 \sqrt{\left(\frac{V_p(z)}{\kappa}\right)^{-2} - p^2} - \sqrt{V_p(z)^{-2} - p^2} dz \quad (5)$$

$$t_2 = \int_{-H}^0 \sqrt{\left(\frac{V_p(z)}{\kappa}\right)^{-2} - p^2} + \sqrt{V_p(z)^{-2} - p^2} dz + \int_{-(H+H_c)}^{-H} \sqrt{\left(\frac{V_p(z)}{\kappa_c}\right)^{-2} - p^2} + \sqrt{V_p(z)^{-2} - p^2} dz \quad (6)$$

$$t_3 = \int_{-H}^0 2\sqrt{\left(\frac{V_p(z)}{\kappa}\right)^{-2} - p^2} dz + \int_{-(H+H_c)}^{-H} 2\sqrt{\left(\frac{V_p(z)}{\kappa}\right)^{-2} - p^2} dz, \quad (7)$$

where  $H_c$  and  $\kappa_c$  are the subsediment crustal thickness and  $V_p/V_s$  determined from eq. (3). In this grid search, we assumed  $V_p$  of the near-surface layer to be  $3 \text{ km s}^{-1}$ . This value is an average of  $V_p$  values of several candidate rocks for the depths of 0–1 km found in Jeju Island (Pliocene marine sediments, tuffs and basalts; Oh *et al.* 2000), following rules for the USGS Bay Area Velocity Model 05.0.0 (Brocher 2005).

In addition, we examined any effects of backazimuthal variations or dipping interface on the layer thickness and its  $V_p/V_s$ . First, we conducted the modified  $H-\kappa$  stacking (eq. 3) for distinct backazimuthal event groups for six stations (JJU, JJB, SS04, SS09, TP08 and TP13) that showed obvious backazimuthal variations in  $Pds$  phase at 3–5 s. Secondly, we examined the effect of the dipping interface beneath the station array by applying the modified  $H-\kappa$  stacking of RFs of the rays traveling along or around the updip directions, as this reduces ambiguity in  $H-\kappa$  stacking results (Wang *et al.* 2010).

### 2.2.3 Common conversion point gathering

Stacking of the RFs typically enhances coherent  $Pds$  conversions while reducing random noise. We applied common conversion point (CCP) stacking (Dueker & Sheehan 1997) to the RFs (for 15 near-surface corrected and 3 uncorrected stations) to further effectively reduce the random noise among stations, which sharply constrained lateral variations of crustal discontinuities beneath the array. In this analysis, the RFs were ray-traced back to their theoretical conversion points and were migrated to depth. We backprojected the RF energy using a modified ak135 global velocity model (Kennett *et al.* 1995) in which the thickness and average  $V_p$  and  $V_s$  of the near-surface sedimentary layer and sub-sediment crust were replaced based on our  $H-\kappa$  stacking results. Accordingly, each station was assigned an individual velocity model. In addition, we also conducted CCP stacking using a fixed model (ak135 global model; Kennett *et al.* 1995) for all the 18 stations to examine the effect of using different velocity models in the stacking.

The study area was gridded into bins of  $0.01^\circ \times 0.01^\circ$ , and a circular cap with a radius of  $0.07^\circ$  was used for gathering and stacking the RF amplitudes. The overlap of the caps serves as a low-pass filter that smooths the subsurface topography of discontinuities, with a corner wavelength approximately equal to the size of the cap (i.e.  $\sim 15$  km; Liu *et al.* 2015). For each bin gridded by  $0.01^\circ \times 0.01^\circ$ , RF amplitudes of the adjacent bins within the cap radius were averaged to represent subsurface seismic structures of that bin. Fig. S1 shows the distribution of the  $P$ -to- $S$  conversion points at depths of 15 and 30 km, which are backprojected using the modified ak135 global velocity model. Notably, CCP stacking can provide some useful information regarding lateral heterogeneities and emphasize near-horizontal structures. Finally, we applied elevation correction using the Shuttle Radar Topography Mission (SRTM3) data set (Farr *et al.* 2007) to accommodate differences in station elevations (<2 km).

## 2.3 RF waveform modelling

To constrain crustal  $V_s$  (and  $V_p/V_s$ ) structure, we performed RF waveform modelling using the RAYSUM wave propagation code (Frederiksen & Bostock 2000). We selected nine stations (PK01, SS02, SS10, TP02, TP04, TP07, TP10, TP11 and TP13; Fig. 2a) that show strong negative RF amplitudes at 1–3 s before positive amplitudes (Fig. S2). Although there can be multiple velocity models to explain our RFs, we explored simple candidate models to better fit such observed amplitudes at mid-to-lower crustal depths.

Each layer in the input model was defined by layer thickness,  $V_p$ ,  $V_s$  and density. We used two types of models in generating synthetic RFs: (1) a two-layer model including crust and mantle and (2) a three-layer model including crust, crustal LVZ and mantle. The density of the LVZ was set as  $2430 \text{ kg m}^{-3}$ . The synthetic RFs are compared against the near-surface corrected RFs for seven stations (SS02, SS10, TP02, TP04, TP07, TP10 and TP13) and uncorrected RFs for two stations (PK01 and TP11).

We set the  $V_p/V_s$  of the entire crust to match the results of  $H-\kappa$  stacking; we set the average crustal  $V_p$  to  $6.3 \text{ km s}^{-1}$ . The  $V_p$  and  $V_s$  of the mantle were set as  $8.04$  and  $4.48 \text{ km s}^{-1}$ , following mantle velocity of the ak135 model (Kennett *et al.* 1995). The thickness of the crust was set to match the  $Pms$  arrival time of data (stacked RFs) using the two-layer model. The densities of crust and mantle were set as  $2700$  and  $3300 \text{ kg m}^{-3}$ , respectively. In our models involving the crustal LVZ, we prescribed the depth to the top interface of the LVZ as determined from the CCP stacking result, and allowed it to vary  $\pm 6$  km from the interface depth in the modelling procedure. The  $V_p$  and  $V_s$  of the upper

**Table 1.** Results of  $H-\kappa$  stacking analysis for the crust and the near-surface sedimentary layer. Crustal thickness ( $H$ ) and  $V_P/V_S$  ( $\kappa$ ) were estimated assuming a mean crustal  $P$  velocity of  $6.3 \text{ km s}^{-1}$  and weighting factors of 0.7, 0.2 and 0.1 for  $Pms$ ,  $PpPms$  and  $PpSms + PsPms$ , respectively. Thickness and  $V_P/V_S$  of the near-surface sedimentary layer were estimated using a mean  $P$  wave velocity of  $3.0 \text{ km s}^{-1}$  and weighting factors of 0.05, 0.7 and 0.25 (Yu *et al.* 2015) for  $Pbs$ ,  $PpPms$  and  $PpSms + PsPms$ , respectively. The uncertainties in layer thicknesses and  $V_P/V_S$  values were estimated from the flatness of the summation function at the maximum using the method of Zhu & Kanamori (2000).

Station	Crustal thickness ( $H$ in km)	Crustal $V_P/V_S(\kappa)$	Sediment thickness (km)	Sediment $V_P/V_S$
JJU <sup>a</sup>	$27.1 \pm 3.7$	$1.570 \pm 0.098$	$1.10 \pm 0.6$	$1.968 \pm 0.297$
JJB <sup>a</sup>	$29.8 \pm 3.0$	$1.760 \pm 0.098$	$1.20 \pm 0.7$	$1.922 \pm 0.197$
HALB <sup>a</sup>	$29.9 \pm 2.8$	$1.683 \pm 0.111$	$1.10 \pm 0.8$	$1.933 \pm 0.205$
PK01	$31.2 \pm 2.3$	$1.778 \pm 0.088$	—	—
SS01	$31.2 \pm 2.1$	$1.755 \pm 0.061$	—	—
SS02 <sup>a</sup>	$28.9 \pm 2.8$	$1.768 \pm 0.069$	$0.80 \pm 0.6$	$3.178 \pm 0.204$
SS04 <sup>a</sup>	$28.1 \pm 2.3$	$1.903 \pm 0.071$	$1.25 \pm 0.7$	$1.873 \pm 0.138$
SS09 <sup>a</sup>	$29.4 \pm 2.2$	$1.838 \pm 0.068$	$0.75 \pm 0.4$	$3.220 \pm 0.217$
SS10 <sup>a</sup>	$27.8 \pm 4.2$	$1.935 \pm 0.061$	$1.05 \pm 1.0$	$2.325 \pm 0.141$
TP01 <sup>a</sup>	$28.1 \pm 2.5$	$1.830 \pm 0.127$	$0.95 \pm 0.5$	$2.083 \pm 0.105$
TP02 <sup>a</sup>	$29.0 \pm 2.5$	$1.698 \pm 0.078$	$0.65 \pm 0.4$	$2.998 \pm 0.200$
TP04 <sup>a</sup>	$28.0 \pm 3.8$	$1.865 \pm 0.122$	$0.75 \pm 0.8$	$2.560 \pm 0.231$
TP07 <sup>a</sup>	$32.0 \pm 2.7$	$1.650 \pm 0.069$	$0.70 \pm 0.5$	$3.325 \pm 0.206$
TP08 <sup>a</sup>	$30.9 \pm 3.0$	$1.708 \pm 0.094$	$0.60 \pm 0.4$	$4.568 \pm 0.243$
TP09 <sup>a</sup>	$29.6 \pm 2.4$	$1.773 \pm 0.074$	$0.85 \pm 0.7$	$2.178 \pm 0.152$
TP10 <sup>a</sup>	$33.5 \pm 2.3$	$1.523 \pm 0.047$	$0.65 \pm 0.4$	$3.000 \pm 0.212$
TP11	$32.4 \pm 2.2$	$1.718 \pm 0.078$	—	—
TP13 <sup>a</sup>	$30.4 \pm 3.1$	$1.685 \pm 0.079$	$0.60 \pm 0.6$	$3.355 \pm 0.615$

<sup>a</sup>Processed with the reverberation removal technique of Yu *et al.* (2015) (Fig. 2a; yellow-outlined squares).

crust were varied within the ranges of  $6.4\text{--}7.0$  and  $3.5\text{--}4.2 \text{ km s}^{-1}$ , respectively, and the  $V_P$  and  $V_S$  of the LVZ were changed accordingly to keep the average crustal  $V_P$  and average crustal  $V_P/V_S$  same as the  $H-\kappa$  stacking result (Table 1).

With these constraints on the input model, we iteratively searched for a model for each station that fits the arrival times and amplitudes of the primary converted phase, in accordance with the approach used by Li *et al.* (2018). We then assessed the quality of the best-fitting model by calculating a maximum correlation in the  $0\text{--}6 \text{ s}$  time window between synthetic R-RFs and data (stacked R-RFs). The time window of  $0\text{--}6 \text{ s}$  was set to compare the arrival times and amplitudes of primary  $Ps$  arrivals from the LVZ and Moho in the data and synthetics, because attenuation or scattering of the later multiples  $> 6 \text{ s}$  may not appear clearly in the data (Chmielowski *et al.* 1999; Janiszewski *et al.* 2013). Furthermore, the arrival times of the first-order multiples from the Moho, arriving outside the time window, were almost the same in all models for each station, because we consistently used the average crustal  $V_P$  and  $V_S$  from the  $H-\kappa$  stacking throughout our modelling procedure.

### 3 RESULTS AND INTERPRETATIONS

#### 3.1 RF images

We first present backazimuthal stacks of RFs for three representative stations, including one permanent (JJU) and two temporary stations (SS04 and TP11) (Fig. 3). In each single-station R-RFs, we observed the largest positive-amplitude  $Pds$  arrival at  $3\text{--}5 \text{ s}$  after  $0 \text{ s}$ , indicating a downward seismic velocity jump at a seismic discontinuity (Figs 3a–c). We regarded this discontinuity as the Moho transition zone beneath Jeju Island. The strong amplitudes arriving at  $3\text{--}5 \text{ s}$  suggest a Moho transition zone with variable topography (Figs 3a–c). At station TP11, we also found a negative-amplitude  $Pds$  signal at  $1\text{--}2 \text{ s}$ , associated with a downward reduction in seismic velocity (Fig. 3c). At station TP11, an additional positive-amplitude signal arrived at  $2 \text{ s}$ , indicating the presence of a localized mid-crustal interface associated with an enhancement of seismic velocity with depth (Fig. 3c).

The R-RFs of stations JJU and SS04 showed strong backazimuthal variation in arrival time of  $Pms$ . The arrival time difference amounted to  $\sim 1 \text{ s}$  in these stations (Figs 3a and b). The R-RFs of station JJU also showed backazimuthal variation in  $Pms$  amplitudes (Fig. 3a). At station JJU, we observed sharp  $Pms$  arrivals at  $3$  and  $4 \text{ s}$  at backazimuths of  $120^\circ\text{--}200^\circ$  and  $30^\circ\text{--}60^\circ$ , respectively (Fig. 3a). The converted amplitude signal became broadened and separated into two ( $3\text{--}5 \text{ s}$ ) between  $200^\circ$  and  $300^\circ$ , indicating a complex, possibly broad, Moho transition zone. These observations are consistent with the findings of a previous RF study at the same station (Jeon *et al.* 2013). At station SS04, the  $Pms$  arrival was observed at  $3.5 \text{ s}$  in the range of backazimuths  $30^\circ\text{--}60^\circ$  and at  $4\text{--}5 \text{ s}$  at other backazimuths (Fig. 3b). In contrast, the R-RFs of station TP11 showed coherent  $Pms$  arrivals at  $\sim 4 \text{ s}$ , regardless of backazimuth (Fig. 3c).

Strong amplitudes in T-RFs were observed at  $\sim 3\text{--}8 \text{ s}$  at station JJU (Fig. 3d) and at fewer than  $\sim 3 \text{ s}$  at station SS04 (Fig. 3e). T-RFs at station TP11 demonstrated a four-lobed backazimuthal polarity flip of  $Pms$  amplitudes at  $\sim 4 \text{ s}$  (Fig. 3f). The amplitudes of T-RFs for station SS08 were larger than those of R-RFs (see station SS08 in Figs S2 and S3 for R-RFs and T-RFs, respectively). These large amplitudes of

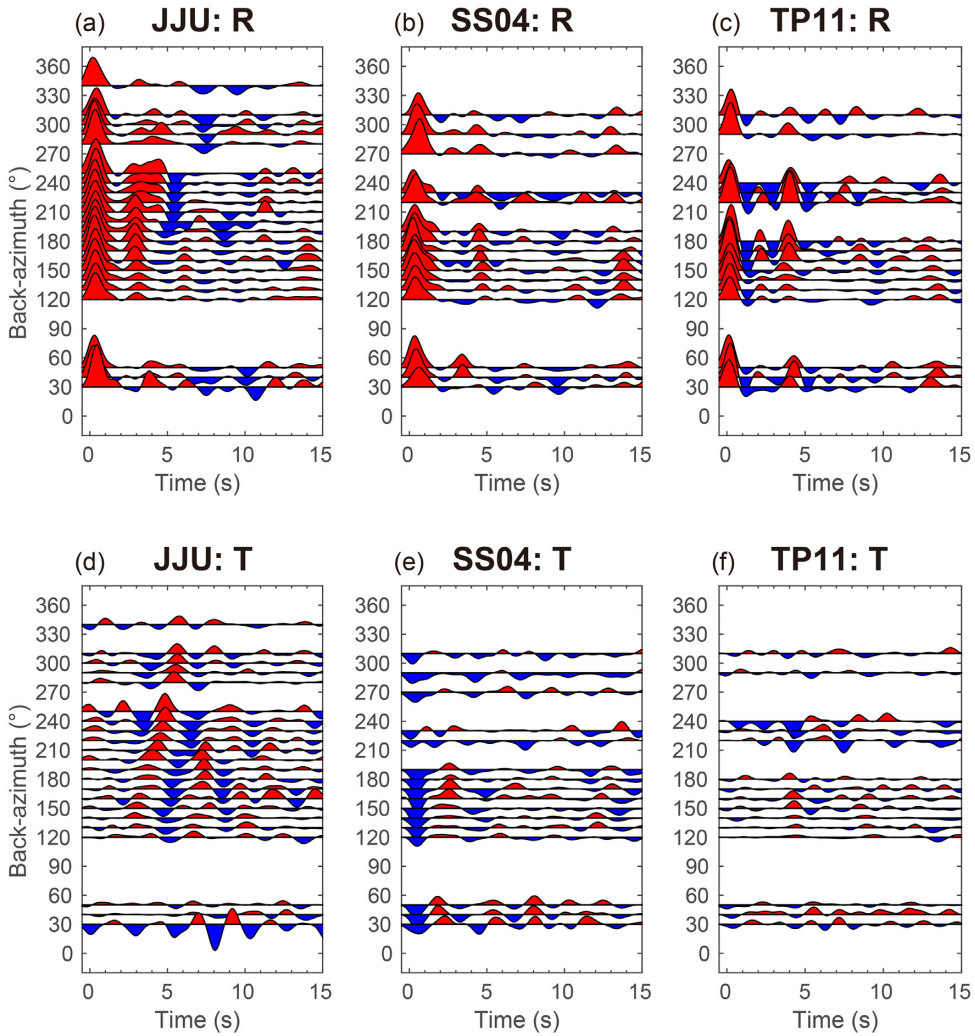


**Figure 3.** Single-station radial (R) and tangential (T) RFs calculated for three representative stations, including one (a, d) permanent (JJU) and two temporary stations (SS04 (b, e) and TP11 (c, f)). Resonance-removal filter is applied to R-RFs of stations JJU and SS04. RFs were stacked by non-overlapping 10° backazimuth bins. Positive amplitudes (red) of R-RFs indicate that impedance increases with depth, while negative amplitudes (blue) indicate that impedance decreases with depth.

T-RFs may have occurred because of inaccurate sensor orientation or problems with the sensor; thus, this station was excluded from further analysis.

The backazimuthal variations of  $P_{ms}$  arrival time and amplitude observed in some stations suggest a local lateral variation in Moho depth and/or the presence of localized anisotropy. In addition, scattering due to heterogeneous crustal structure, including near-surface low-velocity layers (e.g. sediments (Oh *et al.* 2000; Kim & Hong 2012) and volcanic layers (Kwon *et al.* 1993; Lee *et al.* 2007)) and a mid-crustal low-velocity zone (Jeon *et al.* 2013) may contribute to such variations. In this study, we focused on identification of the isotropic seismic structure of the crust; we plan to assess the anisotropic structure of Jeju Island in future studies.

### 3.2 Discontinuity depth and $V_p/V_s$ from $H-\kappa$ stacking method

#### 3.2.1 $H-\kappa$ stacking results of the crust

The  $H-\kappa$  stacking results showed small degrees of variation in both crustal thickness ( $H$ ) and crustal  $V_p/V_s$  ( $\kappa$ ) with different weight sets (Table S3). The largest differences were found at station TP13 ( $\Delta H = 0.7$  km,  $\Delta \kappa = 0.037$ ), which implied a complex crustal structure beneath station TP13. Because the  $H-\kappa$  results were generally consistent regardless of weight sets, we selected the results obtained with the weighting factors ( $w_1 = 0.7$ ,  $w_2 = 0.2$  and  $w_3 = 0.1$ ) for presentation and interpretation of our results.

Fig. 4 shows examples of  $H-\kappa$  stacking of the RFs for two stations located near each other ( $\sim 13$  km apart): TP07 and SS09. The estimated crustal thicknesses for the two stations were  $32.0 \pm 2.7$  and  $29.4 \pm 2.2$  km, respectively (Figs 4a and d).  $V_p/V_s$  values considerably differed between these two stations ( $1.650 \pm 0.069$  and  $1.838 \pm 0.068$ , respectively, Figs 4a and d). Although the output of  $H-\kappa$  stacking may

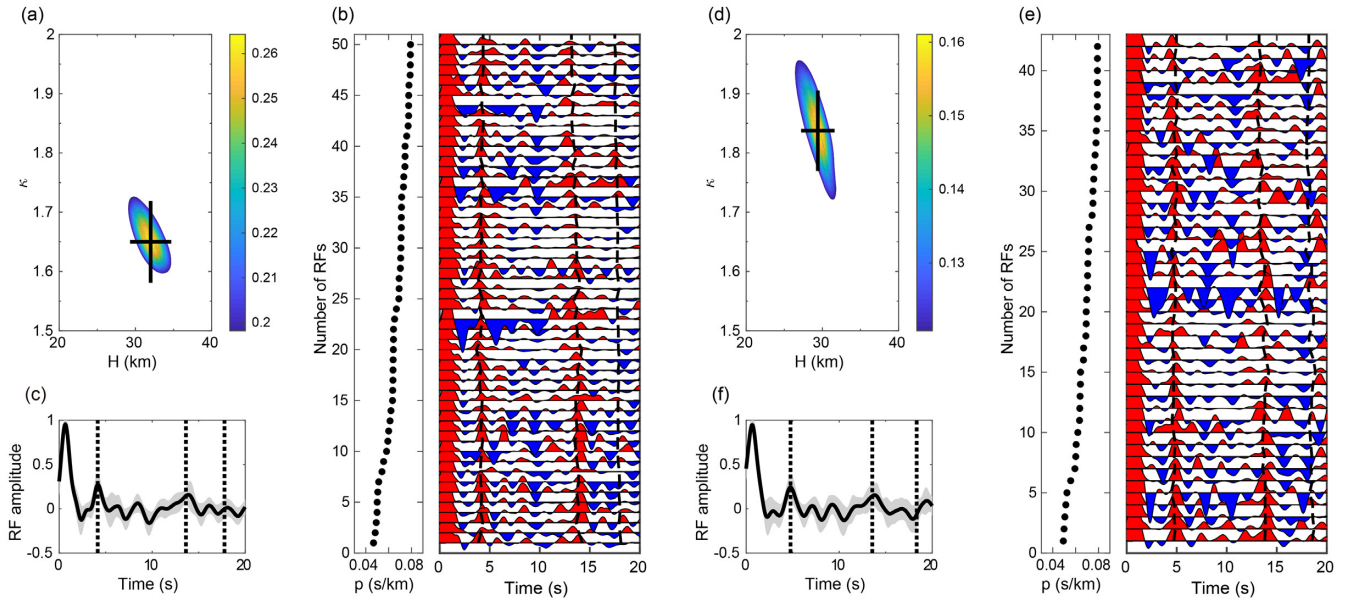


**Figure 4.** Examples of  $H$ - $\kappa$  stacking results for two stations, TP07 and SS09. (a, d) Contour maps of optimal  $H$  and  $\kappa$  values determined for stations (a) TP07 and (d) SS09. Weighting factors for  $P_{ms}$  and its multiples ( $P_{pPms}$  and  $P_{sPms} + P_{pSms}$ ) are 0.7, 0.2 and 0.1, respectively. Black crosses represent uncertainties of optimal  $H$  and  $\kappa$  values. (b, e) RFs of stations (b) TP07 and (e) SS09, sorted according to the ray parameter ( $p$ ). Predicted arrival times of  $P_{ms}$  and its multiples ( $P_{pPms}$  and  $P_{sPms} + P_{pSms}$ ) are indicated by black dashed lines. (c, f) Stacked RF traces are shown as black lines; averaged predicted arrival times of  $P_{ms}$ ,  $P_{pPms}$  and  $P_{sPms} + P_{pSms}$  of the stations (c) TP07 and (f) SS09 are indicated by black dashed lines. Individual RFs were normalized before stacking. Grey shading indicates one standard deviation of the RF stacks.

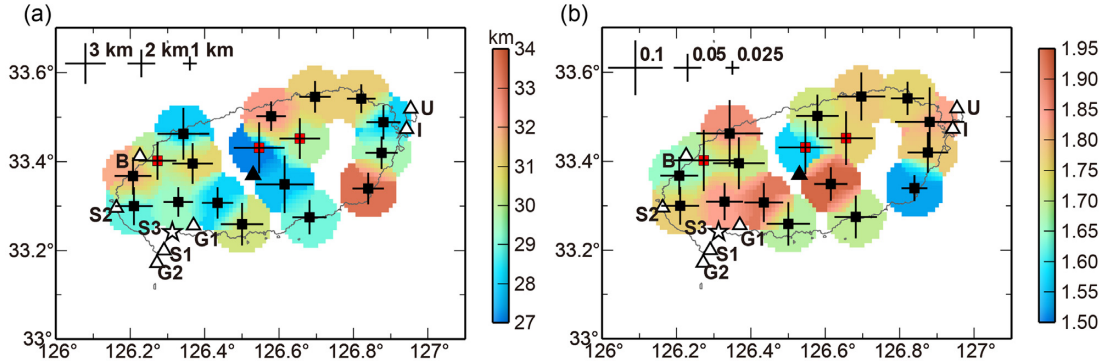


**Figure 5.** Crustal thickness (a) and crustal  $V_P/V_S$  (b) determined by  $H$ - $\kappa$  stacking of RFs for individual stations, using unequal weighting factors of  $w_1 = 0.7$ ,  $w_2 = 0.2$  and  $w_3 = 0.1$ . The uncertainties of optimal  $H$  and  $\kappa$  values for individual stations (Table 1) are shown as black crosses, with their sizes proportional to magnitude. The results from the  $H$ - $\kappa$  stacking method were interpolated using weights inversely proportional to the square of the uncertainty estimates and the distance from the stations, within ray sampling radius ( $\sim 7.4$  km) from the stations.  $H$ - $\kappa$  results for stations with fewer than 15 RF traces were excluded to avoid uncertainties resulting from limited numbers of RFs. Symbol definitions are provided in legend for Fig. 2(a). See Fig. S5 for non-interpolated version.

be nonunique partly due to nonuniform backazimuthal distribution of event data,  $V_P/V_S$  estimates for these two stations were robust given the quality of the data and their uncertainty estimates. In addition to a very clear and coherent Moho conversion ( $P_{ms}$ ) at  $\sim 4\text{--}5$  s in the individual traces (Figs 4b and e), as well as in the stacked traces (Figs 4c and f), the multiple phases from the Moho ( $P_{pPms}$  and  $P_{pSms} + P_{sPms}$ ) were also clear (Figs 4b, c and e and f).

The  $H$ - $\kappa$  stacking results for 18 stations are shown in Table 1 and Fig. S4. The stacking provided crustal thicknesses between 27.1 and 33.5 km, with an average thickness of 29.9 km (Figs 5a and S5a). Stations in central (JJU, SS04 and SS10), northwestern (TP04), and eastern Jeju (TP01) showed thin crustal thicknesses of 27.1–28.1 km (Table 1).

Crustal  $V_P/V_S$  values for all stations ranged from 1.523 to 1.935, with an average crustal  $V_P/V_S$  of 1.747 (Figs 5b and S5b). In particular, the crustal thickness estimates for two permanent stations (JJU and JJB) were  $27.1 \pm 3.7$  and  $29.8 \pm 3.0$  km, respectively, while  $V_P/V_S$  values were  $1.570 \pm 0.098$  and  $1.760 \pm 0.098$ , respectively (Table 1 and Fig. S4). Our estimates of the crustal thickness for those two stations were thinner than previous estimates by Jeon *et al.* (2013): 29 and 33 km for stations JJU and JJB, respectively. The  $V_P/V_S$  estimates by Jeon *et al.* (2013) were 1.64 (JJU) and 1.75 (JJB). Jeon *et al.* (2013) did not consider the effect of the near-surface structure, and this can lead to slightly thicker crustal thickness estimates and can affect the crustal  $V_P/V_S$  values. Regardless of such difference, the trend of the values is consistent.

Variations in  $V_p/V_s$  values were considerable throughout the island (Fig. 5b). High  $V_p/V_s$  values were present in the eastern (1.830 at station TP01), northwestern (1.865 at station TP04), and southern (1.903 at station SS04, 1.838 at station SS09 and 1.935 at station SS10) parts of Jeju Island. Abnormally low  $V_p/V_s$  values were present in the central (1.57 at station JJU) and southeastern (1.523 at station TP10) parts of Jeju Island (Figs 5b and S5b). Stations with low  $V_p/V_s$  were located around the western (1.683 at HALB, 1.650 at TP07 and 1.708 at station TP08), northern (1.718 at station TP11), southern (1.685 at TP13 and 1.698 at TP02) margins of Jeju Island.

In particular, station TP10 shows three local maxima of  $s(H, \kappa)$  in  $H-\kappa$  stacking after the resonance-removal correction to the RFs, indicating the presence of complex crustal structure (Fig. S4). Although we selected the largest maximum ( $H = 33.5 \pm 2.3$  km,  $\kappa = 1.523 \pm 0.047$ ) as the preferred solution, there are two other probable solutions, which indicate thinner crust ( $H = 26.1 \pm 2.1$  km or  $28.8 \pm 2.3$  km) with higher  $V_p/V_s$  ratio ( $\kappa = 1.683 \pm 0.057$  or  $1.918 \pm 0.088$ ) than our selected values. Notably,  $H-\kappa$  results can be highly dependent on the choice of stacking and data parameters. Such parameters include relative weights assigned to the Moho  $P$ -to- $S$  conversion and its reverberations, the choice of linear or phase-weighted stacking, input crustal  $V_p$ , RF frequency content, and the number of RFs analysed (Ogden *et al.* 2019).

### 3.2.2 Effects of a dipping interface

$H-\kappa$  stacking of the RFs yielded an average crustal thickness and  $V_p/V_s$  value, indicative of an isotropic homogeneous layer. For the six stations that showed clear backazimuthal variations of  $P_{ms}$  arrivals, the crustal thickness and crustal  $V_p/V_s$  estimates deviated among backazimuthal groups (Table S4 and Fig. S6), indicating the presence of anisotropy and/or dip. In particular, the two permanent stations (JJU and HALB) showed 360° cycle polarity variation of direct  $P$  in T-RFs from positive to negative at 300° and 120° (Fig. S3), respectively, indicating the presence of a dipping interface (Wang *et al.* 2010). However, for stations JJU and HALB, the estimated crustal thickness and  $V_p/V_s$  did not change significantly, regardless of different event sets (differences less than 0.2 km and 0.005 in crustal thickness and  $V_p/V_s$ , respectively, Table S5). Therefore, the effect of the dipping interface can be considered minor in our data set.

### 3.2.3 $H-\kappa$ stacking results of the near-surface layer

The thickness and  $V_p/V_s$  of the near-surface sedimentary layer for the 15 stations ranged between 0.6–1.25 km and 1.873–4.568, respectively (Table 1 and Fig. S7). The observed thickness of the low-velocity near-surface layer is roughly consistent with previous studies that reported near-surface low-velocity layers with thicknesses of several hundred metres (Kim & Hong 2012; Oh *et al.* 2000). The observed high  $V_p/V_s$  values can be caused by unconsolidated sedimentary layer, as also observed at Powder River Basin, northern Wyoming, US and at Songliao Basin, northeast China (Yu *et al.* 2015). Assuming that the  $V_p$  of the near-surface layer is 3 km s<sup>-1</sup>, the observed low  $V_s$  values (0.7–1.7 km s<sup>-1</sup>) of the layer is similar to the previous  $V_s$  estimates of 0.6–1.1 km s<sup>-1</sup>, reported for the marine sediments Jeju Island (Kim & Hong 2012).

## 3.3 CCP images

The CCP images along eight profiles depicted clear lateral variations in crustal structure (Fig. 6). Fig. S1 shows the event distribution of the  $Pds$  conversion points at depths of 15 and 30 km beneath Jeju Island. Our images revealed two distinct discontinuities, at depth of 8–30 km and 26–40 km (Fig. 6). The shallow discontinuity delineated by negative RF amplitudes marked the upper boundary of the seismic LVZ. The average depth to the top interface of the LVZ was 17.4 km. This interface is deeper (20–30 km depth) in the western and southeastern parts of Jeju Island and shallower (8–11 km depth) in the northeastern part (Fig. 7a). The deep discontinuity delineated by positive RF amplitudes marked the Moho transition zone. The average Moho depth was 33.5 km. Strong amplitudes were present at a shallow depth (26–29 km) beneath the central and southern parts of the island (Fig. 7b). The observed amplitude variations did not mirror the surface topography of Jeju Island [Fig. 7b; see images for profiles BB' (Fig. 6b), EE' (Fig. 6e), GG' (Fig. 6g) and HH' (Fig. 6h)]. Beneath the summit of Mt Halla, the Moho depth was 28 km (Fig. 7b).

In addition to the observed complex topography for the Moho transition zone and the top of the LVZ, the amplitudes of the  $Pds$  phase also varied spatially. The map of amplitude variations for the top of the LVZ showed relatively large values concentrated in the coastal regions of the island, especially in the northern part (Fig. 7c). On the other hand, large positive amplitude anomalies were observed in central Jeju Island beneath Mt Halla (Fig. 7d). Such variations in the amplitudes of the  $Pds$  phase can be also observed in the single-station R-RFs (Fig. S2).

The converted phase amplitudes indicated impedance contrast across the discontinuity, and more critically a change in  $V_s$  values across the discontinuity (Kim *et al.* 2010, 2012). Therefore, this amplitude information can provide useful constraints regarding lithology. However, the interpretation may be complex, because the amplitudes depend on the backazimuthal distribution of the earthquakes used in the analysis and/or sharpness of the discontinuity. We assumed that amplitude variations due to azimuthal coverage could be suppressed, because we used average amplitudes taken from the CCP stacks of the RFs for interpretation.

Comparing our CCP image derived from individual velocity models (Figs 6 and 7) with that from one fixed model (ak135 model, Figs S10 and S11), we found that the depth to the crustal discontinuities (Moho and TLVZ) differ by a few kilometres, especially in the southern flank of Jeju. Regardless of the different models used in the stacking, we observed that RF amplitude variations at the Moho depths and

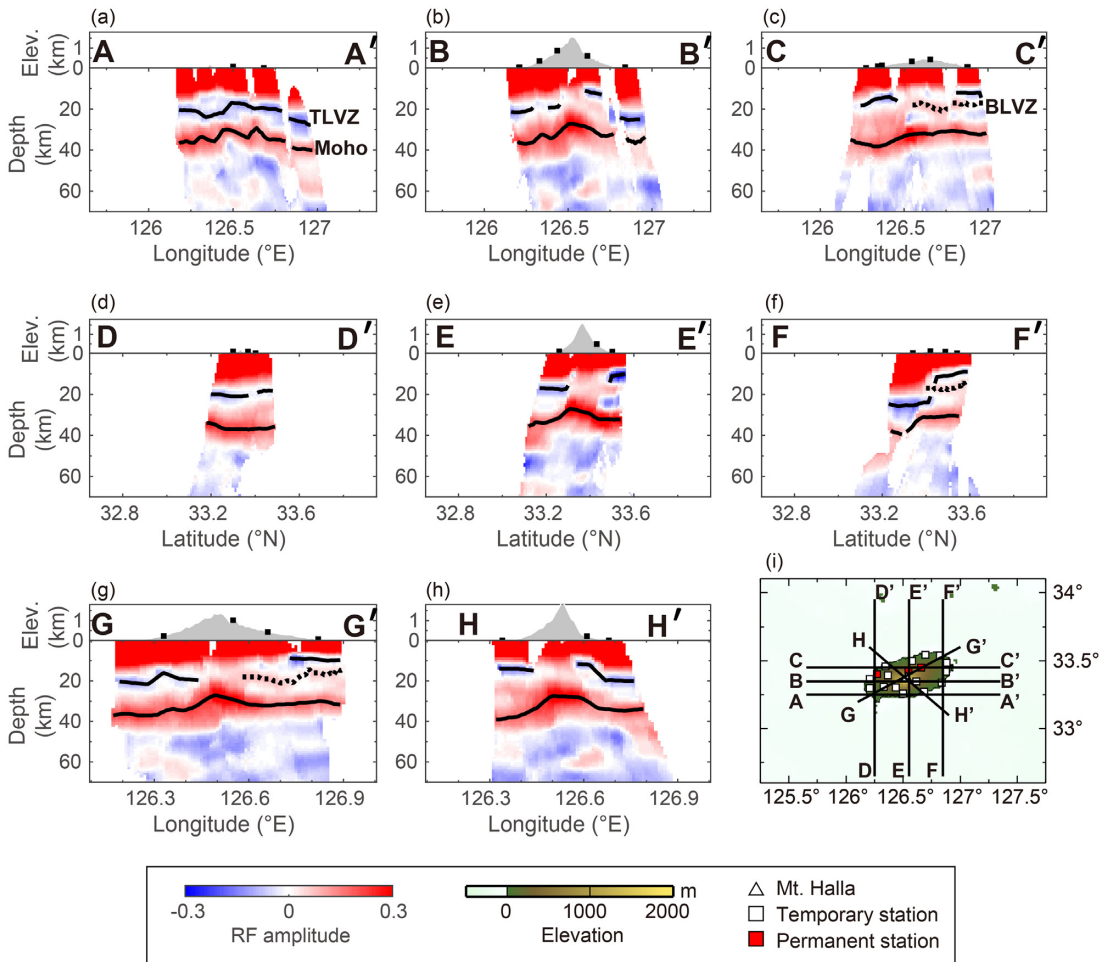


**Figure 6.** CCP images along eight profiles: (a) AA', (b) BB', (c) CC', (d) DD', (e) EE', (f) FF', (g) GG' and (h) HH'. The locations of the profiles are shown in (i). Red and blue indicate impedance increase and decrease with depth, respectively. Top panel in each figure shows surface topography with station locations (squares). Black solid lines in each panel indicate the top interfaces of LVZ (TLVZ) and Moho. Black dotted lines in panels c, f and g indicate the bottom interfaces of LVZ (BLVZ). The black solid lines in panels a–h mark the maximum (Moho) or minimum (TLVZ) amplitude of CCP stacked RFs at crustal depth range; the black dotted lines (BLVZ) in panels c, f and g mark the maximum amplitude of CCP stacked RFs at mid-crustal depth range. Grids with more than 15 piercing points are presented (Fig. S1).

top of the LVZ are similar. Both models show complex Moho topography and the presence of mid-to-lower crustal low-velocity zone in the peripheral areas of Jeju.

### 3.4 RF waveform modelling results

RF modelling for the nine stations indicated that models including the LVZ at mid-crustal depth produced the best-fitting synthetic RFs with the highest correlation coefficient in the 0–6 s time window (Fig. 8). The models including the LVZ explained well strong negative RF signals at 1–3 s, whereas the models without the LVZ failed to fit the observed negative arrivals and yielded a lower correlation coefficient (Fig. 8). The best-fitting models for the nine stations showed the LVZ with low  $V_S$  values ( $2.69\text{--}3.95 \text{ km s}^{-1}$ ;  $3.2 \text{ km s}^{-1}$  in average) and a wide range of  $V_P/V_S$  values (1.521–2.06; 1.845 in average) with its top interface at depth of 10–30 km (Fig. 9). The  $V_P/V_S$  values were high (1.765–2.06; 1.885 in average) except for one station (1.521 at TP10) that showed very low average crustal  $V_P/V_S$  (1.523, Table 1). Excluding the station TP10 which showed  $V_S$  of  $3.95 \text{ km s}^{-1}$ , the  $V_S$  value of the LVZ ( $2.69\text{--}3.47 \text{ km s}^{-1}$ ) is slower than the typical  $V_S$  of lower continental crust ( $3.51\text{--}4.15 \text{ km s}^{-1}$ ; Rudnick & Fountain 1995). The elevated  $V_P/V_S$  values of the LVZ presumably support the existence of partial melting and/or aqueous fluids, because their presence generally increases the  $V_P/V_S$  values (Kim *et al.* 2013; Kim & Clayton 2015).

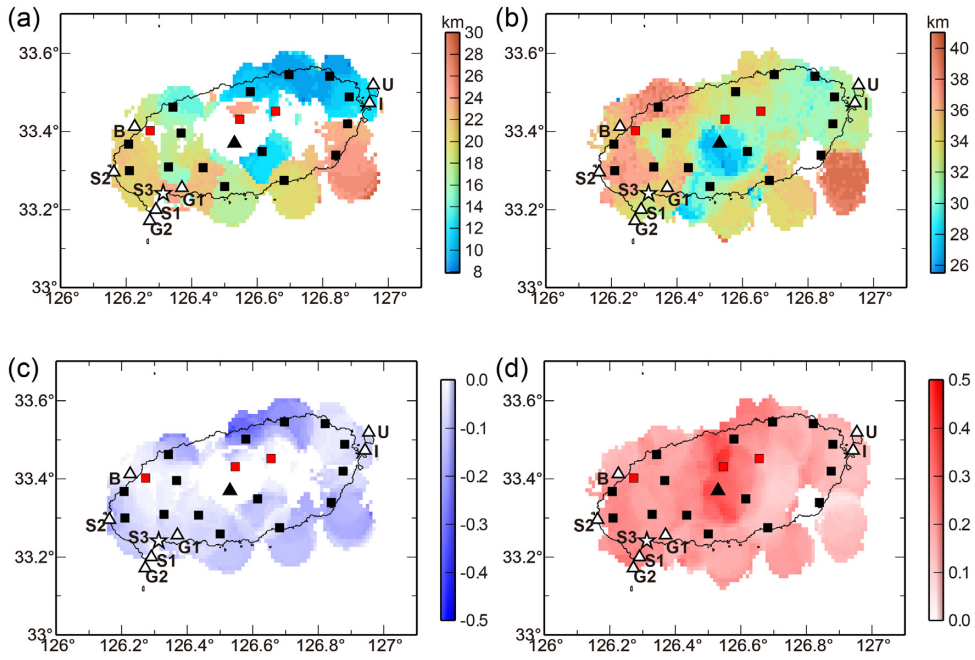


**Figure 7.** Variation in discontinuity depths and amplitudes of CCP stacks. (a) Topography of the top of the LVZ obtained from CCP stacks. (b) Moho topography obtained from CCP stacks. (c) Normalized amplitudes at the top of the LVZ. (d) Normalized amplitudes at the Moho. Only bins with more than 15 piercing points are shown in the figure. See Fig. S9 for results using different minimum numbers of piercing points within a bin (20, 30 and 40). Symbol definitions are provided in legend for Fig. 2(a).

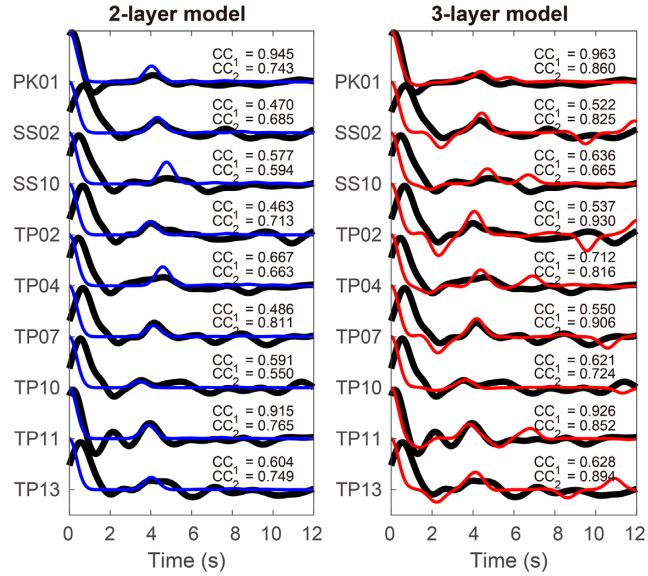


**Figure 8.** Comparison between stacked R-RFs using all events (data; thick black traces) and synthetic R-RFs for nine stations. We used two models in generating the synthetic R-RFs: one model without crustal LVZ (2-layer model; thin blue traces) and the other model with the LVZ (3-layer model; thin red traces). Correlation coefficients between data and the synthetic R-RFs from the models in the 0–6 s time window ( $CC_1$ ) and a narrower time window including  $P_{LVZ}$  and  $P_{ms}$  (1–5 s for PK01 and TP11 and 1.5–5 s for the other seven stations) ( $CC_2$ ) are shown on the upper right corner of each trace.

## 4 DISCUSSION

### 4.1 Complex Moho transition zone topography

The results of  $H-\kappa$  and CCP stacking revealed a complex topography of the Moho transition zone under Jeju Island (Figs 5a and 7b). The two different results showed similar characteristics of the shallow Moho transition zone at depth of  $\sim 27$  km, near Mt Halla (Figs 5a and 7b). However, the average Moho depths were found  $\sim 3$  km deeper in the CCP results for the whole island.  $H-\kappa$  stacking is generally useful for the estimation of average Moho depth below a station; however, in our study, it primarily reflected the structure in the southern and southeastern parts of each station because teleseismic earthquake locations were predominantly distributed in these backazimuths. CCP stacking provided

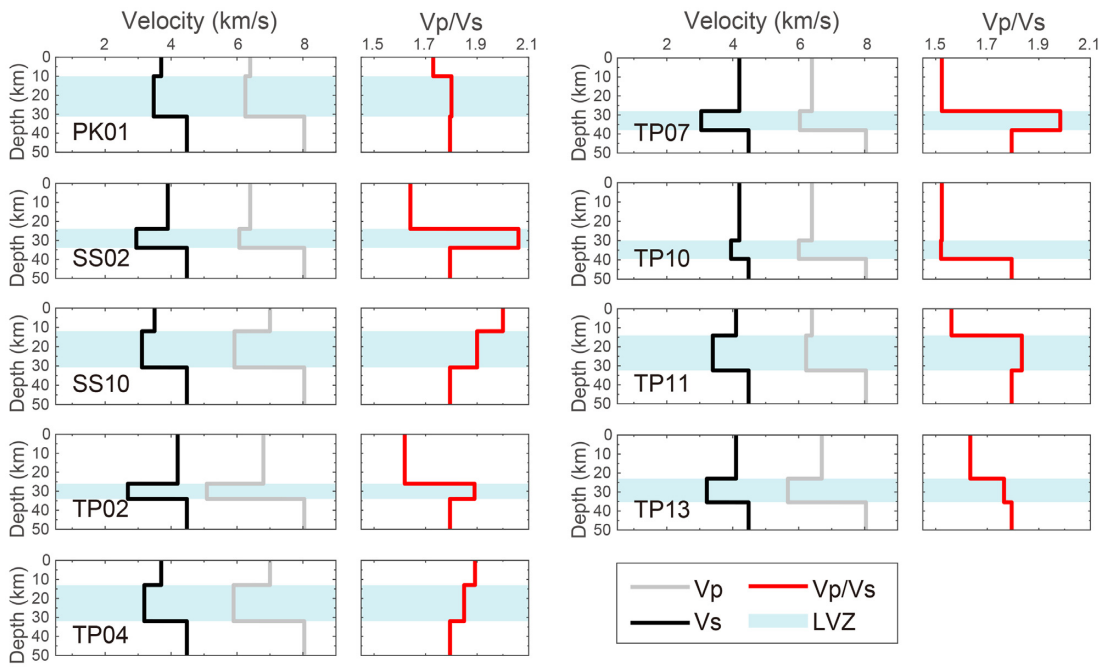


**Figure 9.** Best-fitting velocity models used in generating the synthetic RFs for the nine stations shown in Fig. 8.  $V_P/V_S$  values for the nine stations were estimated from the best-fitting  $V_P$  and  $V_S$  models.

better spatial resolution than  $H-\kappa$  stacking in our study because station separation distance (average 9 km in this study) was much smaller than the lateral conversion offset ( $\sim 20$  km) at the Moho depth (Rondenay 2009).

The observed complex Moho topography can be inferred from the backazimuthal differences in the arrival times of the  $P_{ms}$  phase shown in individual RF traces (Figs 3 and 10a). For example, in station SS04, the converted waves sampling northeast (backazimuth range of  $20^\circ$ – $50^\circ$ ) mostly arrive much earlier ( $\sim 3$  s) than those sampling other backazimuths (4–5 s, Fig. 10b). These observed  $P_{ds}$  arrival time differences can either be attributed to lateral variations in seismic velocity structure and/or to discontinuity depth (e.g. Janiszewski *et al.* 2020).

We consider the observed variation in the  $P_{ms}$  arrival time to mainly result from Moho topography, rather than lateral variation of the crustal velocity structure only. Assuming a uniform Moho depth of 30 km, the observed  $P_{ms}$  arrival time can be explained by a rapid average crustal velocity in central Jeju Island (northeast of station SS04; G3) and a slow velocity in southern Jeju Island (south of station SS04; G2, Fig. 10c). Assuming instead constant crustal  $P$ - and  $S$ -wave velocity of the ak135 model (Kennett *et al.* 1995), Moho depth varies with different backazimuths from 29 to 48 km beneath station SS04 (Fig. 10d). Considering that the previous local velocity model of Song *et al.* (2018) for Jeju showed the opposite trend of  $V_S$  structure to that shown in Fig. 10(c) beneath central Jeju Island at depths  $< 30$  km, the Moho topography is likely a critical factor affecting the  $P_{ms}$  arrival times.

Notably, existence of mafic cumulates at the base of the crust may also have an effect on the Moho depth estimates, which will be discussed further in Section 4.2. In Jeju Island, xenoliths of mafic cumulates have been found in lavas, which indicate intrusions of basaltic magmas in the lower part of the crust (Yang 2004; Yang *et al.* 2012b). A subcrustal intrusive complex can contribute to large velocity contrast, leading to large amplitude signals in teleseismic images.

In addition, the presence of shallow anisotropic layers, observed by ambient noise analysis (Lee *et al.* 2021), may increase the uncertainty in Moho depth estimates. Other potential sources of errors in this study include the insufficient number of events and incomplete event backazimuthal coverage for several temporary seismic stations, due to the short operation period (Table S1).

## 4.2 Seismic crustal structure beneath Mt Halla

In typical volcanic zones, a thick crustal root is often observed and is attributed to a magmatic addition to the crust beneath the volcano (Thybo & Artemieva 2013). Beneath Mt Baekdu (also known as Changbaishan; a Cenozoic intraplate volcano in northeast Asia), a thick crust ( $\sim 40$  km) is reported to result from mafic underplating at the bottom of the crust (Kim *et al.* 2017). In Jeju Island, xenoliths of mafic cumulates are found in lavas (Yang 2004; Yang *et al.* 2012b), consistent with observations of mafic cumulates in other volcanic regions. However, as shown by our teleseismic images (Figs 6b, e, g and h), the strong amplitude signals are found below the summit of Mt Halla, at shallower depths compared to the surroundings (Figs 7b and d). The depth to the top of the Moho transition zone is 26–29 km below the central part of the island and Mt Halla (1947 m above sea level, Fig. 7b).

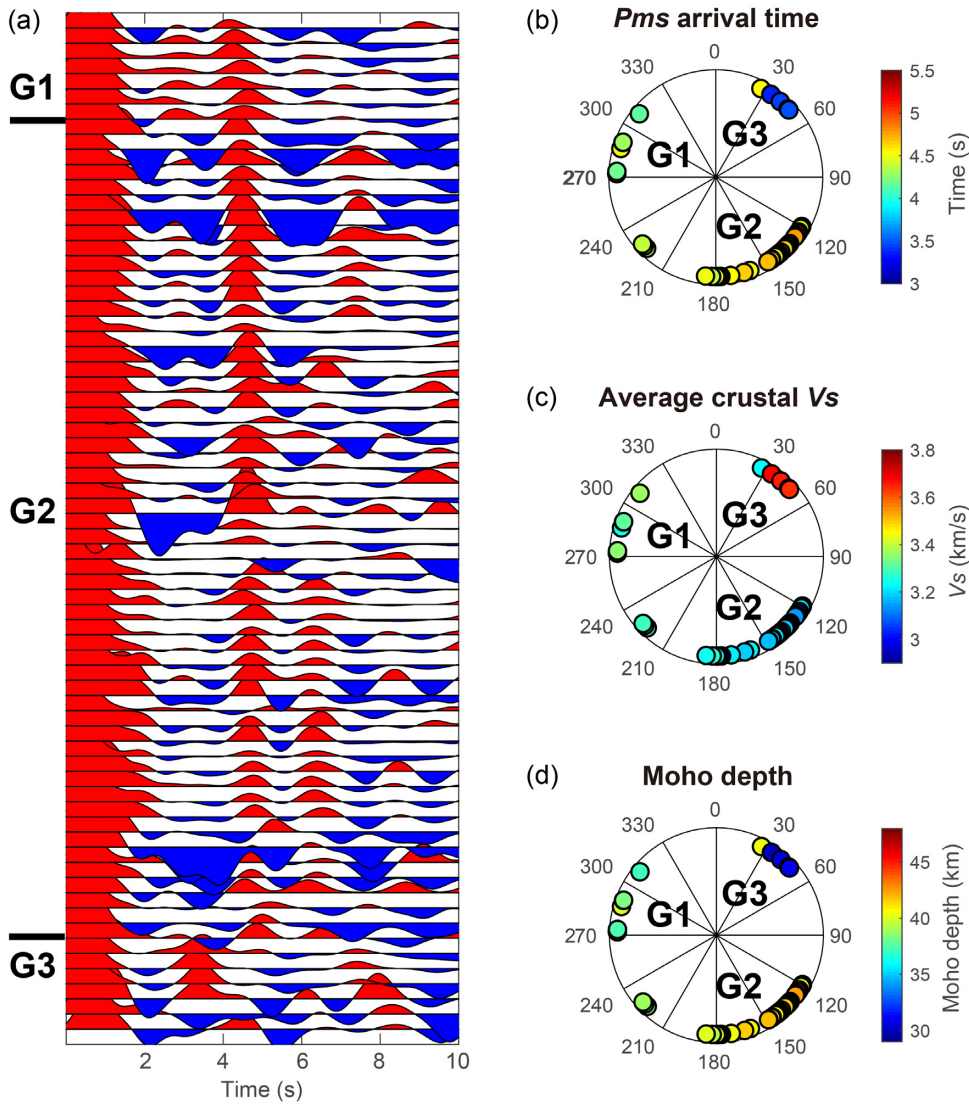


**Figure 10.** (a) Near-surface corrected, single-station RF traces for station SS04, according to backazimuth. (b) Variation in  $P_{ms}$  arrival time, plotted along the ray backazimuth. (c) Average crustal  $V_s$  values near station SS04 plotted along the ray backazimuth, assuming a uniform Moho depth of 30 km. (d) Distribution of Moho depth plotted along the ray backazimuth, assuming a constant velocity structure (ak135 global velocity model; Kennett *et al.* 1995) beneath the station SS04. Three different backazimuthal groups (G1, G2 and G3) are highlighted in the figure. Backazimuthal ranges for G1, G2 and G3 are  $270^\circ$ – $310^\circ$ ,  $110^\circ$ – $230^\circ$  and  $20^\circ$ – $50^\circ$ , respectively.

If the strong seismic signals at a depth of 26–29 km arise from sharp Moho discontinuities, crustal thinning by 5–8 km ( $\sim 1/5$  of the crust) would imply a tectonic setting such as a rift, for which there is no evidence in the continental shelf where Jeju Island is located. The magma plumbing system may cause large variations in the observed crustal thickness. Mushy hot zones near the base of the crust can be closely associated with the voluminous magma supply that built Mt Halla in the centre of the island (Fig. 11). In this context, the presence of mafic cumulates represents the crust-mantle transition zone (e.g. Ding *et al.* 2019); this mafic layer may contribute to the large velocity contrast with the felsic crust above central Jeju Island, but small velocity contrast with ultramafic upper mantle beneath central Jeju Island.

Teleseismic traveltimes data suggest a sub-lithospheric magmatic structure below the summit of Mt Halla (Fig. 11; Song *et al.* 2018). Based on the velocity model described by Song *et al.* (2018), a focused decompression melting at sub-lithospheric depths and complex magma interactions within the lithosphere presumably explain the intraplate magmatic activities of Jeju Island (Song *et al.* 2018). This suggests that hot and buoyant mantle can support the high elevations of Mt Halla. The support of thin crust by hot asthenospheric material has also been reported in the Central Alborz mountains in western Asia (Sodoudi *et al.* 2009). Finally, the strong amplitude of  $Pds$  beneath Mt Halla (Fig. 7d) may be related to residual heat or fluids from the recent (25 ka) episode of trachyte volcanism that formed the top of Jeju Island (Brenna *et al.* 2015).

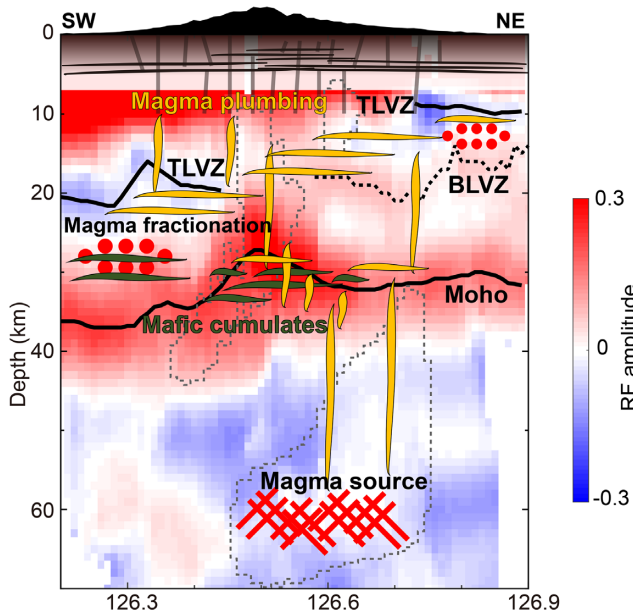


**Figure 11.** Teleseismic imaging results combined with schematic interpretation of upper crust (Lee *et al.* 2021), crust (this work) and uppermost mantle (Song *et al.* 2018) magma plumbing structures informed by petrological constraints (Brenna *et al.* 2012b). The profile line is parallel to GG' shown in Fig. 6. Black solid lines indicate the top interfaces of LVZ (TLVZ) and Moho. The black dotted line indicates the bottom interfaces of LVZ (BLVZ). Thin grey dashed lines enclose low  $P$ -wave velocity anomalies ( $< -0.7$  per cent) constrained by Song *et al.* (2018). Red hatched area represents the magma source and red circles represent the magma fractionation areas suggested by Brenna *et al.* (2012b). The relatively active plumbing system with melt/mushy dikes and sills (orange) and old cumulate and intrusive bodies (dark green) are superimposed on the RF image. The shallow magma plumbing system consisting of a layered structure of sill and dike is located up to a depth of 10 km in the crust of Jeju Island (Lee *et al.* 2021). The elevation of Jeju Island is exaggerated by 2.5 times.

#### 4.3 Mid-to-lower crustal low-velocity zone in peripheral area of Jeju

Using ambient noise data, Lee *et al.* (2021) imaged upper crustal (1–10 km) radially anisotropic structures beneath Jeju Island. Their images indicated dike swarms at depths of 1–2 and 5–10 km, covering the top and bottom of sill structures at depths of 2–5 km (Fig. 11). These structures were interpreted as pathways that supply magma to the shallow crust from deeper reservoirs.

In this study, we observed a strong negative-amplitude signal at 1–3 s in our RF images from 9 out of 18 stations, and these nine stations are located in the coastal regions of Jeju Island (Fig. 2a). The RF modelling of such strong negative-amplitude signal requires an LVZ in the mid-to-lower crust at a depth of 10–40 km. Our RF waveform modelling revealed that  $V_S$  estimates of the LVZ were  $3.2 \text{ km s}^{-1}$  on average; these values were similar to those previously reported by Jeon *et al.* (2013) ( $3.2 \pm 0.1 \text{ km s}^{-1}$ ). The  $V_P/V_S$  of the LVZ was estimated to be 1.765–2.06 (except for station TP10). Variability in low  $V_S$  and high  $V_P/V_S$  values for individual stations indicates melt and crystal mushes present. We note that the negative-amplitude signal is absent or weak at other nine stations (JJU, JJB, HALB, SS01, SS04, SS09, TP01, TP08 and TP09) (see Fig. S2a for station SS01 and Fig. S2b for the other eight stations).

Several stations in Jeju Island (e.g. station TP11, Fig. 3c) showed a series of negative-positive amplitude signals at 1–3 s, which were considered to be the converted signals at the top and bottom interfaces of the LVZ. Most stations that showed a series of negative-positive amplitude signals at 1–3 s were distributed in the northeastern part of Jeju Island. The mid-crustal discontinuity indicating the bottom of the LVZ was also clearly visible in the CCP cross-sections along the profiles CC', FF' and GG' (Figs 6c, f and g, respectively). The velocity transition from the top of the LVZ to the Moho may be gradual in stations that showed only negative amplitude signals at 1–3 s.

Several previous studies indicated LVZs in the middle or lower crust, beneath or near volcanoes, in both intraplate and plate boundary settings. The presence of an LVZ beneath Mt Baekdu, an intraplate volcano, was characterized by studies using RFs (Hetland *et al.* 2004), ambient noise (Kim *et al.* 2017), joint inversion of RFs and ambient noise (Zhu *et al.* 2019), and 3-D deep seismic sounding (Zhang *et al.* 2002). LVZs were also found in arc volcanoes (e.g. Mt Fuji) by RFs (Kinoshita *et al.* 2015) and seismic tomography (Nakamichi *et al.* 2007) and in the Aleutian Islands by RFs (Janiszewski *et al.* 2013). The LVZ is typically understood to include magmatic reservoirs consisting of mechanically weak materials (e.g. partial melts/crystal mushes and/or aqueous fluids, Abe *et al.* 2010; Sudo & Kong 2001).

Our imaged LVZ implies the presence of a series of magma reservoirs connecting the deep sublithospheric magma source region with the shallow (depth  $< 10$  km) plumbing system of Jeju Island, as proposed in previous geochemical and petrological studies (Brenna *et al.* 2012b; Yang *et al.* 2012a, Fig. 11). The spatially distributed depth profile of the LVZ supports a dispersed plumbing system feeding the  $>300$  eruptive vents on Jeju Island, rather than a focused central plumbing system beneath Mt Halla (Brenna *et al.* 2012b). The low  $V_S$  (average of  $3.2 \text{ km s}^{-1}$ ) and high  $V_P/V_S$  (average of 1.845) values associated with the LVZ (Fig. 9) may indicate different degrees of melt present in partly crystallized dyke/sill networks.

#### 4.4 Variations of crustal $V_P/V_S$

Laboratory experiments have shown that the mineralogical composition and melting condition of crustal rocks are the main determining factors for the bulk crustal Poisson's ratio or  $V_P/V_S$  (e.g. Christensen 1996; Christensen & Mooney 1995). Our  $H-\kappa$  analysis showed that crustal  $V_P/V_S$  values vary widely beneath Jeju Island (1.523–1.935), with an average crustal  $V_P/V_S$  value of 1.747 (Fig. 5b). This average estimate is lower than the average continental value of 1.78 (Zandt & Ammon 1995); it may not accurately represent a volcanic region, because the presence of partial melt and/or fluids generally increases  $V_P/V_S$  (Kim *et al.* 2010, 2012, 2013; Kim & Clayton 2015). Thus, the  $V_P/V_S$  estimate for an individual station is more meaningful for interpretation of spatial variations, rather than for interpretation of the average value. Notably, the trade-off between crustal thickness ( $H$ ) and  $V_P/V_S$  ( $\kappa$ ) in the  $H-\kappa$  stacking may add uncertainty in the obtained crustal  $V_P/V_S$  values in our study. In addition, the estimates of  $\kappa$  (and to a lesser degree  $H$ ) can be markedly biased in the presence of anisotropy (Kaviani & Rümpker 2015).

Typically,  $V_P/V_S$  values are inversely related to the silica content of the medium (Zandt & Ammon 1995). Basalts and trachytes erupted on Jeju Island have a wide range of silica content (44–66 per cent) (Brenna *et al.* 2012b). These diverse lithologies associated with volcanism, as well as the granitic basement, may explain our observed  $V_P/V_S$  range. As shown in Fig. 5(b), the distribution of  $V_P/V_S$  estimates varied considerably among stations. This distribution of  $V_P/V_S$  values may be related to the plumbing system of dispersed small-volume volcanoes distributed throughout the island, which may be closely linked to different degrees of magma evolution.

High  $V_P/V_S$  values are found in southwestern parts of the island, where older trachytes (700–800 ka) are located (Sanbangsan region; S3); in contrast, relatively lower  $V_P/V_S$  value is found in the central part of the island (Fig. 5b). Based on these data, an older (700–800 ka) solidified plumbing system with mafic cumulates and plutonic rocks beneath the Sanbangsan region may contribute to the higher  $V_P/V_S$  values in the southwestern parts of the island (Fig. 11). Conversely the younger plumbing system associated with the Halla trachytes remains warm and partly mushy, resulting in the lower  $V_P/V_S$  in the central parts of the island. In addition, the diverse  $V_P/V_S$  values throughout Jeju Island may indicate the heterogeneous density and distribution of the basaltic plumbing system over the island. Stations with low  $V_P/V_S$  may indicate greater abundance of quartz-rich felsic crust.

## 5 CONCLUSIONS

We investigated the deep crustal seismic structure beneath the Jeju Island intraplate volcanic field formed by Pleistocene to Holocene eruptions, based on teleseismic RFs. To improve imaging of the Moho geometry, we first eliminate the effect of complex near-surface structure in RFs and then migrated RFs to a depth of 0–70 km by using the CCP stacking approach. We also used a grid-search scheme to constrain the seismic discontinuity depth and  $V_P/V_S$  values by stacking the RF amplitudes at predicted arrival times for the  $P$ -to- $S$  converted phase and its multiples for different values of layer thickness and  $V_P/V_S$ . Our teleseismic images revealed a clear interface of the Moho transition zone beneath Jeju Island and a mid-to-lower crustal LVZ beneath the coastal region of the island. The depths to the two interfaces were highly variable (top interface of LVZ at a depth of 8–30 km and deeper crustal interface at a depth of 26–40 km) over a short distance (< 75 km). The observed topography of the Moho transition zone suggested crustal thinning below Mt Halla. Considering the tectonic setting of Jeju Island on the continental shelf, the Moho topography may be indicative of a layered crust-mantle transition zone composed of mafic cumulates and partially molten mushes. The diversity of crustal  $V_P/V_S$  values (1.523–1.935) indicates heterogeneous crustal compositions beneath the island. Our imaged LVZ suggests an extensively distributed magma plumbing system, with magma batches stalling and evolving in the lower crust, resulting in the chemical diversity of magmas observed on Jeju Island.

## ACKNOWLEDGEMENTS

The temporary seismic array in Jeju was a collaborative effort between Seoul National University (SNU) and Pukyong National University (PNU). Authors are grateful to people who deployed and maintained the network for 2 yr. Also, authors thank H. Lim (SNU) for providing angles for sensor orientation corrections for permanent stations, J.-H. Song for the 3-D velocity model of the upper mantle beneath Jeju and S.-J. Lee for the 3-D velocity model of the upper crust beneath Jeju. Data from the KIGAM and KMA were retrieved from the National Earthquake Comprehensive Information System (NECIS) website (in Korean, last accessed 2019/07) upon approval. YK, JR and T-S Kang acknowledge support from Development of unified 3-D seismic velocity model program (KMI2019-00110) through Korea Meteorological Administration. HK and YK acknowledge the National Research Foundation of Korea (NRF) grant funded by the Korea government (MSIT, No. NRF-2019R1G1A1094833). Finally, the authors thank Editor Ian Bastow, Christian Stanciu and an anonymous reviewer for comments which greatly improved this paper.

## DATA AVAILABILITY

The data underlying this paper will be shared on reasonable request to the corresponding author.

## REFERENCES

- Abe, Y., Ohkura, T., Shibusaki, T., Hirahara, K. & Kato, M., 2010. Crustal structure beneath Aso Caldera, Southwest Japan, as derived from receiver function analysis, *J. Volc. Geotherm. Res.*, **195**, 1–12.
- Ahn, U.S., 2016. Study of the last volcanic activity on historical records on Jeju Island, Korea, *J. Petrol. Soc. Korea*, **25**, 69–83.
- Ammon, C.J., 1991. The isolation of receiver effects from teleseismic P waveforms, *Bull. seism. Soc. Am.*, **81**, 2504–2510.
- Annen, C., Blundy, J. & Sparks, R., 2005. The genesis of intermediate and silicic magmas in deep crustal hot zones, *J. Petrol.*, **47**, 505–539.
- Bannister, S., Bryan, C. J. & Bibby, H. M., 2004. Shear wave velocity variation across the Taupo Volcanic Zone, New Zealand, from receiver function inversion, *Geophys. J. Int.*, **159**(1), 291–310.
- Bianchi, I., Park, J., Piana Agostinetti, N. & Levin, V., 2010. Mapping seismic anisotropy using harmonic decomposition of receiver functions: an application to Northern Apennines, Italy, *J. geophys. Res.*, **115**, B12317..
- Bird, P., 2003. An updated digital model of plate boundaries, *Geochem. Geophys. Geosyst.*, **4**, 1027.
- Brenna, M., Cronin, S.J., Smith, I.E., Sohn, Y.K. & Németh, K., 2010. Mechanisms driving polymagmatic activity at a monogenetic volcano, Udo, Jeju Island, South Korea, *Contrib. Mineral. Petrol.*, **160**, 931–950.
- Brenna, M., Cronin, S.J., Smith, I.E., Maas, R. & Sohn, Y.K., 2012a. How small-volume basaltic magmatic systems develop: a case study from the Jeju Island Volcanic Field, Korea, *J. Petrol.*, **53**, 985–1018.
- Brenna, M., Cronin, S.J., Smith, I.E., Sohn, Y.K. & Maas, R., 2012b. Spatio-temporal evolution of a dispersed magmatic system and its implications for volcano growth, Jeju Island Volcanic Field, Korea, *Lithos*, **148**, 337–352.
- Brenna, M., Cronin, S.J., Keresztsuri, G., Sohn, Y.K., Smith, I.E. & Wijbrans, J., 2015. Intraplate volcanism influenced by distal subduction tectonics at Jeju Island, Republic of Korea, *Bull. Volcanol.*, **77**, 7.
- Brocher, T.M., 2005. Compressional and shear wave velocity versus depth in the San Francisco Bay Area, California: rules for USGS Bay area velocity model 05.0.0, U.S. Geol. Surv. Open-File Rept. 05–1317.
- Chang, S.-J. & Baag, C.-E., 2006. Crustal structure in southern Korea from joint analysis of regional broadband waveforms and travel times, *Bull. seism. Soc. Am.*, **96**, 856–870.
- Chang, S.-J. & Baag, C.-E., 2007. Moho depth and crustal Vp/Vs variation in southern Korea from teleseismic receiver functions: implication for tectonic affinity between the Korean Peninsula and China, *Bull. seism. Soc. Am.*, **97**, 1621–1631.
- Chmielowski, J., Zandt, G. & Haberland, C., 1999. The central Andean Altiplano-Puna magma body, *Geophys. Res. Lett.*, **26**(6), 783–786.
- Choi, J.-H., Kim, H.-J., Nam, M.-J., Lee, T.-J., Han, N.-R., Lee, S.-K., Song, Y.-H. & Suh, J.-H., 2007. A study on geoelectrical structure of Jeju island using 3D Mt inversion of 2D profile data, *Geophys. Geophys. Explor.*, **10**, 268–274.
- Christensen, N.I., 1996. Poisson's ratio and crustal seismology, *J. geophys. Res.*, **101**, 3139–3156.
- Christensen, N.I. & Mooney, W.D., 1995. Seismic velocity structure and composition of the continental crust: a global view, *J. geophys. Res.*, **100**, 9761–9788.
- Ding, S., Ni, S., Kim, Y. & He, X., 2019. Constraints on crust-mantle transition zone with Pn waveforms: a case study of eastern China and southern Korean Peninsula, *Phys. Earth planet. Inter.*, **289**, 11–19.
- Dueker, K.G. & Sheehan, A.F., 1997. Mantle discontinuity structure from midpoint stacks of converted P to S waves across the Yellowstone hotspot track, *J. geophys. Res.*, **102**, 8313–8327.
- Farr, T.G. *et al.* 2007. The shuttle radar topography mission, *Rev. Geophys.*, **45**, 1–13.
- Frederiksen, A. W. & Bostock, M. G., 2000. Modelling teleseismic waves in dipping anisotropic structures, *Geophys. J. Int.*, **141**(2), 401–412.
- Hetland, E., Wu, F. & Song, J., 2004. Crustal structure in the Changbaishan volcanic area, China, determined by modeling receiver functions, *Tectonophysics*, **386**, 157–175.
- Janiszewski, H.A., Abers, G.A., Shillington, D.J. & Calkins, J.A., 2013. Crustal structure along the Aleutian island arc: new insights from receiver functions constrained by active-source data, *Geochem. Geophys. Geosyst.*, **14**, 2977–2992.
- Janiszewski, H.A., Wagner, L.S. & Roman, D.C., 2020. Aseismic mid-crustal magma reservoir at Cleveland Volcano imaged through novel receiver function analyses, *Sci. Rep.*, **10**, 1–9.
- Jeon, T., Kim, K.Y. & Woo, N., 2013. S-wave velocities beneath Jeju Island, Korea, using inversion of receiver functions and the H- $\kappa$  stacking method, *Geophys. Geophys. Explor.*, **16**, 18–26.
- Kang, H. & Kim, Y., 2019. Localized anisotropic subduction-zone structure in Southern Peru: constraints from teleseismic receiver functions and forward modeling, *Seismol. Res. Lett.*, **90**, 1820–1835..
- Kang, S., 2003. Benthic foraminiferal biostratigraphy and paleoenvironments of the Seogwipo Formation, Jeju Island, Korea, *J. Paleontol. Soc. Korea*, **19**, 63–153.
- Kaviani, A. & Rümpker, G., 2015. Generalization of the H- $\kappa$  stacking method to anisotropic media, *J. geophys. Res.*, **120**, 5135–5153.
- Keating, G.N., Valentine, G.A., Krier, D.J. & Perry, F.V., 2008. Shallow plumbing systems for small-volume basaltic volcanoes, *Bull. Volcanol.*, **70**, 563–582.
- Kennett, B.L., Engdahl, E. & Buland, R., 1995. Constraints on seismic velocities in the Earth from traveltimes, *Geophys. J. Int.*, **122**, 108–124.
- Kim, J.-I., Choi, S.H., Koh, G.W., Park, J.B. & Ryu, J.-S., 2019. Petrogenesis and mantle source characteristics of volcanic rocks on Jeju Island, South Korea, *Lithos*, **326**, 476–490.
- Kim, K.Y. & Hong, M.H., 2012. Shear-wave velocity structure of Jeju Island, Korea, *Geosci. J.*, **16**, 35–45.
- Kim, S., Tkalcic, H. & Rhee, J., 2017. Seismic constraints on magma evolution beneath Mount Baekdu (Changbai) volcano from transdimensional Bayesian inversion of ambient noise data, *J. geophys. Res.*, **122**, 5452–5473.
- Kim, Y., Clayton, R. & Jackson, J., 2010. Geometry and seismic properties of the subducting Cocos plate in central Mexico, *J. geophys. Res.*, **115**(B6), doi:10.1029/2009JB006942 .
- Kim, Y., Clayton, R.W. & Jackson, J.M., 2012. Distribution of hydrous minerals in the subduction system beneath Mexico, *Earth planet. Sci. Lett.*, **341**, 58–67.
- Kim, Y., Clayton, R.W., Asimow, P.D. & Jackson, J.M., 2013. Generation of talc in the mantle wedge and its role in subduction dynamics in central Mexico, *Earth planet. Sci. Lett.*, **384**, 81–87.
- Kim, Y. & Clayton, R.W., 2015. Seismic properties of the Nazca oceanic crust in southern Peruvian subduction system, *Earth planet. Sci. Lett.*, **429**, 110–121.
- Kim, Y., Lee, C. & Kim, S.-S., 2015. Tectonics and volcanism in East Asia: insights from geophysical observations, *J. Asian Earth Sci.*, **113**, 842–856.
- Kinoshita, S., Igarashi, T., Aoki, Y. & Takeo, M., 2015. Imaging crust and upper mantle beneath Mount Fuji, Japan, by receiver functions, *J. geophys. Res.*, **120**, 3240–3254.
- Kiyosugi, K., Connor, C.B., Wetmore, P.H., Ferwerda, B.P., Germa, A.M., Connor, L.J. & Hintz, A.R., 2012. Relationship between dike and volcanic conduit distribution in a highly eroded monogenetic volcanic field: San Rafael, Utah, USA, *Geology*, **40**, 695–698.
- Koh, G.-W. & Park, J.-B., 2010. The study on geology and volcanism in Jeju Island (III): early lava effusion records in Jeju Island on the basis of  $^{40}\text{Ar}/^{39}\text{Ar}$  absolute ages of lava samples, *Econ. Environ. Geol.*, **43**, 163–176.
- Koh, G.-W., Park, J.-B., Kang, B.-R., Kim, G.-P. & Moon, D.C., 2013. Volcanism in Jeju Island, *J. Geol. Soc. Korea*, **49**, 209–230.
- Kwon, B.-D., Chung, H.-J. & Lee, H.-S., 1993. Physical properties of volcanic rocks in Chejudo, *J. Korean Earth Sci. Soc.*, **14**, 348–357.
- Kwon, B.-D., Lee, H.-S., Jung, G.-G. & Chung, S.-W., 1995. Investigation of subsurface structure of Cheju Island by gravity and magnetic methods, *Econ. Environ. Geol.*, **28**, 395–404.
- Langston, C.A., 1979. Structure under Mount Rainier, Washington, inferred from teleseismic body waves, *J. geophys. Res.*, **84**, 4749–4762.

- Lee, C.-S., Cho, T.-C., Lee, S.-B. & Won, K.-S., 2007. A study of weathering characteristic of Baeknokdam trachyte in Jeju Island, *J. Eng. Geol.*, **17**, 235–251.
- Lee, K., Jeong, B.I., Choi, K.S. & Lee, S.K., 1983. A study of gravity and geomagnetism of Jeju Island, *J. Geol. Soc. Korea*, **19**, 1–10.
- Lee, K. & Kim, H., 1993. Deep electrical soundings in the Cheju island, *J. Geol. Soc. Korea*, **29**, 30–38.
- Lee, S.-J., Kim, S., Rhie, J., Kang, T.-S. & Kim, Y., 2021. Upper crustal shear wave velocity and radial anisotropy beneath Jeju Island volcanoes from ambient noise tomography, *Geophys. J. Int.*, **225**(2), 1332–1348.
- Li, H., Wei, M., Li, D., Liu, Y., Kim, Y. & Zhou, S., 2018. Segmentation of slow slip events in south central Alaska possibly controlled by a subducted oceanic plateau, *J. geophys. Res.*, **123**(1), 418–436.
- Ligorria, J.P. & Ammon, C.J., 1999. Iterative deconvolution and receiver-function estimation, *Bull. seism. Soc. Am.*, **89**, 1395–1400.
- Lim, H., Kim, Y., Song, T.-R.A. & Shen, X., 2018. Measurement of seismometer orientation using the tangential P-wave receiver function based on harmonic decomposition, *Geophys. J. Int.*, **212**, 1747–1765.
- Liu, Z. et al. 2015. Receiver function images of the mantle transition zone beneath NE China: new constraints on intraplate volcanism, deep subduction and their potential link, *Earth planet. Sci. Lett.*, **412**, 101–111.
- Muirhead, J.D., Van Eaton, A.R., Re, G., White, J.D. & Ort, M.H., 2016. Monogenetic volcanoes fed by interconnected dikes and sills in the Hopi Buttes volcanic field, Navajo Nation, USA, *Bull. Volcanol.*, **78**, 11.
- Nakamichi, H., Watanabe, H. & Ohminato, T., 2007. Three-dimensional velocity structures of Mount Fuji and the South Fossa Magna, central Japan, *J. geophys. Res.*, **112**, B03310.
- Ogden, C. S., Bastow, I. D., Gilligan, A. & Rondenay, S., 2019. A reappraisal of the  $H\text{-}\kappa$  stacking technique: implications for global crustal structure, *Geophys. J. Int.*, **219**(3), 1491–1513.
- Oh, J., Yi, S., Yoon, S., Koh, G.W., Yun, H. & Lee, J.D., 2000. Subsurface stratigraphy of Jeju Island, *J. Geol. Soc. Korea*, **36**, 181–194.
- Rondenay, S., 2009. Upper mantle imaging with array recordings of converted and scattered teleseismic waves, *Surv. Geophys.*, **30**, 377–405.
- Rudnick, R.L. & Fountain, D.M., 1995. Nature and composition of the continental crust: a lower crustal perspective, *Rev. Geophys.*, **33**, 267–309.
- Shin, Y.H., Choi, K.S., Koh, J.S., Yun, S.H., Nakamura, E. & Na, S.H., 2012. Lithospheric-folding-based understanding on the origin of the backarc basaltic magmatism beneath Jeju volcanic island, *Tectonics*, **31**, TC4005.
- Sodoudi, F., Yuan, X., Kind, R., Heit, B. & Sadikhouy, A., 2009. Evidence for a missing crustal root and a thin lithosphere beneath the Central Alborz by receiver function studies, *Geophys. J. Int.*, **177**, 733–742.
- Sohn, Y.K. & Park, K.H., 2004. Early-stage volcanism and sedimentation of Jeju Island revealed by the Sagye borehole, SW Jeju Island, Korea, *Geosci. J.*, **8**, 73.
- Sohn, Y.K., Park, K.H. & Yoon, S.H., 2008. Primary versus secondary and subaerial versus submarine hydrovolcanic deposits in the subsurface of Jeju Island, Korea, *Sedimentology*, **55**, 899–924.
- Sohn, Y.K. & Yoon, S.-H., 2010. Shallow-marine records of pyroclastic surges and fallouts over water in Jeju Island, Korea, and their stratigraphic implications, *Geology*, **38**, 763–766.
- Song, J.-H., Kim, S., Rhie, J., Lee, S.-H., Kim, Y. & Kang, T.-S., 2018. Imaging of lithospheric structure beneath Jeju Volcanic Island by teleseismic traveltome tomography, *J. geophys. Res.*, **123**, 6784–6801.
- Sudo, Y. & Kong, L., 2001. Three-dimensional seismic velocity structure beneath Aso Volcano, Kyushu, Japan, *Bull. Volcanol.*, **63**, 326–344.
- Suhardja, S. K., Widiyantoro, S., Métaxian, J. P., Rawlinson, N., Ramdhani, M. & Budi-Santoso, A., 2020. Crustal thickness beneath Mt. Merapi and Mt. Merbabu, Central Java, Indonesia, inferred from receiver function analysis, *Phys. Earth planet. Inter.*, **302**, 106455.
- Tatsumi, Y., Shukuno, H., Yoshikawa, M., Chang, Q., Sato, K. & Lee, M.W., 2005. The petrology and geochemistry of volcanic rocks on Jeju Island: plume magmatism along the Asian continental margin, *J. Petrol.*, **46**, 523–553.
- Thybo, H. & Artemieva, I.M., 2013. Moho and magmatic underplating in continental lithosphere, *Tectonophysics*, **609**, 605–619.
- Venzke, E., 2013. Global Volcanism Program. Volcanoes of the World, v. 4.8.5 (30 December 2019), Smithsonian Institution. Downloaded 09 Feb 2020, doi:10.5479/si.GVP.VOTW4-2013.
- Wang, P., Wang, L., Mi, N., Liu, J., Li, H., Yu, D., Xu, M., Wang, X. & Guo, Z., 2010. Crustal thickness and average  $V_p/V_s$  ratio variations in southwest Yunnan, China, from teleseismic receiver functions, *J. geophys. Res.*, **115** (B11).
- Yang, K., 2004. Fluid inclusions trapped in xenoliths from the lower crust/upper mantle beneath Jeju Island (I): a preliminary study, *J. Petrol. Soc. Korea*, **13**, 34–45.
- Yang, K., Arai, S., Yu, J.-E., Yun, S.-H., Kim, J.-S. & Hwang, J.-Y., 2012a. Gabbroic xenoliths and megacrysts in the Pleisto-Holocene alkali basalts from Jeju Island, South Korea: the implications for metasomatism of the lower continental crust, *Lithos*, **142**, 201–215.
- Yang, K., Szabó, C., Arai, S., Yu, J.-E. & Jung, H., 2012b. Silica enrichment of Group II xenoliths by evolved alkali basalt from Jeju Island, South Korea: implication for modification of intraplate deep-seated rocks, *Mineral. Petrol.*, **106**, 107–130.
- Yeck, W. L., Sheehan, A. F. & Schulte-Pelkum, V., 2013. Sequential  $H\text{-}\kappa$  stacking to obtain accurate crustal thicknesses beneath sedimentary basins, *Bull. seism. Soc. Am.*, **103**(3), 2142–2150.
- Yoo, H., Herrmann, R., Cho, K. & Lee, K., 2007. Imaging the three-dimensional crust of the Korean Peninsula by joint inversion of surface-wave dispersion and teleseismic receiver functions, *Bull. seism. Soc. Am.*, **97**, 1002–1011.
- Yu, Y., Song, J., Liu, K. H. & Gao, S. S., 2015. Determining crustal structure beneath seismic stations overlying a low-velocity sedimentary layer using receiver functions, *J. geophys. Res.*, **120**(5), 3208–3218.
- Zandt, G. & Ammon, C.J., 1995. Continental crust composition constrained by measurements of crustal Poisson's ratio, *Nature*, **374**, 152–154.
- Zelt, B. C. & Ellis, R. M., 1998. Receiver-function studies in the Trans-Hudson orogen, Saskatchewan, *Can. J. Earth Sci.*, **36**(4), 585–603.
- Zhang, X.-k. et al. 2002. Deep seismic sounding investigation into the deep structure of the magma system in Changbaishan-Tianchi volcanic region, *Acta Seismol. Sin.*, **15**, 143–151.
- Zhu, H., Tian, Y., Zhao, D., Li, H. & Liu, C., 2019. Seismic structure of the Changbai intraplate volcano in NE China from joint inversion of ambient noise and receiver functions, *J. geophys. Res.*, **124**, 4984–5002.
- Zhu, L. & Kanamori, H., 2000. Moho depth variation in southern California from teleseismic receiver functions, *J. geophys. Res.*, **105**, 2969–2980.

## SUPPORTING INFORMATION

Supplementary data are available at *GJI* online.

**Table S1.** Station name, network ID, time period and number of earthquakes at individual stations used to generate RFs in this study.

**Table S2.** Orientation correction angles determined by Lim *et al.* (2018) for the permanent stations in Jeju. Orientation angle ranges from 0° to 360° in the clockwise direction; each value indicates the angle rotation needed relative to misaligned North.

**Table S3.** Results of  $H\text{-}\kappa$  stacking, computed using four sets of unequal weighting factors (WS1, WS2, WS3 and WS4) in the stacking of  $Pds$ ,  $PpPds$  and  $PpSds+PsPds$  phases.

**Table S4.** Results of  $H\text{-}\kappa$  stacking analysis for different backazimuthal groups for six stations with obvious backazimuthal variations of  $Pms$  arrivals in RFs (Fig. S6). Crustal thickness ( $H$ ) and  $V_p/V_s$  ( $\kappa$ ) were estimated assuming a mean crustal  $V_p$  of 6.3 km s<sup>-1</sup> and weighting

factors of 0.7, 0.2 and 0.1 for  $Pms$ ,  $PpPms$  and  $PpSms+PsPms$ , respectively; uncertainties were estimated from the flatness of the summation function at the maximum, using the method of Zhu & Kanamori (2000). Backazimuth ranges ( $\Phi$ ) for G1, G2 and G3 for each station are listed in the table.

**Table S5.** Comparison of  $H-\kappa$  stacking results for two stations (JJU and HALB) using all RF traces and selected RF traces for rays traveling in the updip direction only.

**Figure S1.** Distribution of  $Pds$  conversion points in the study region.  $Pds$  conversion points at depths of (a) 15 km and (b) 30 km are shown as blue 'X's. Locations of temporary and permanent broad-band seismic stations are shown as black and red squares, respectively. RFs for the 18 stations used in  $H-\kappa$  stacking were also used in CCP stacking.

**Figure S2.** Single-station R-RFs for all stations used in this study. RFs were stacked by  $10^\circ$  backazimuth bins with no overlap. (a) Single-station R-RFs for 23 stations without near-surface correction. (b) Single-station R-RFs for 15 stations after applying the resonance removal filter to correct for the near-surface structure. Positive amplitudes (red) indicate that impedance increases with depth, whereas negative amplitudes (blue) indicate that impedance decreases with depth.

**Figure S3.** Single-station T-RFs for all stations used in this study. RFs were stacked by  $10^\circ$  backazimuth bins with no overlap.

**Figure S4.**  $H-\kappa$  stacking results for the 18 stations used in this study. Unequal weighting factors of  $w_1 = 0.7$ ,  $w_2 = 0.2$  and  $w_3 = 0.1$  were used for  $Pms$ ,  $PpPms$  and  $PpSms + PsPms$  phases, respectively. See Fig. 4 for detailed information for the plotting scheme, and also see Fig. S8 for the single station RFs for the 18 stations used in the  $H-\kappa$  stacking.

**Figure S5.** Crustal thickness (a) and crustal  $V_P/V_S$  (b) determined by  $H-\kappa$  stacking of RFs for individual stations. The uncertainties of optimal  $H$  and  $\kappa$  values for individual stations (Table 1) are shown as black crosses, with their sizes proportional to their magnitudes.  $H-\kappa$  results for stations with fewer than 15 RF traces were excluded to avoid uncertainties resulting from limited numbers of RFs. Black triangles indicate the summit of Jeju Island, Mt Halla. See Fig. 5 for interpolated version. Locations of recently erupted (<25 ka) small-scale volcanoes (B, Biyangdo; S1, Songaksan; S2, Suwolbong; I, Ilchulbong; U, Udo; G1, Gunsan; G2, Gapado; Ahn 2016) are shown as white triangles and denoted by their abbreviations. Location of trachyte volcano, Sanbangsan (S3), is indicated by a white star.

**Figure S6.** R-RFs for six stations (JJU, JJB, SS04, SS09, TP08 and TP13) stacked by non-overlapping  $10^\circ$  backazimuthal bins. Resonance-removal filter is applied to all R-RFs of the six stations. Background colours indicate three backazimuthal groups (G1, pink; G2, orange; G3, brown).  $H-\kappa$  stacking was applied to different backazimuthal groups for each station; these results are summarized in Table S4.

**Figure S7.**  $H-\kappa$  stacking results for near-surface sedimentary layer for the 15 stations used in this study. Unequal weighting factors of  $w_4 = 0.05$ ,  $w_2 = 0.7$  and  $w_3 = 0.25$  were used for  $Pbs$ ,  $PpPms$  and  $PpSms + PsPms$  phases, respectively.

**Figure S8.** Single-station RFs for the 18 stations, sorted according to the ray parameter ( $p$ ). A resonance-removal filter (Yu *et al.* 2015) was applied to individual RFs for the 15 stations (JJU, JJB, HALB, SS02, SS04, SS09, SS10, TP01, TP02, TP04, TP07, TP08, TP09, TP10 and TP13) to remove the effects of a low-velocity sedimentary layer (see Table 1). Predicted arrival times of  $Pms$  and its multiples ( $PpPms$  and  $PpSms + PsPms$ ) are indicated by black dashed lines.

**Figure S9.** Variations in discontinuity depths and amplitudes of CCP stacks. (a-c) Topography of the top of the LVZ obtained from CCP stacks. (d-f) Normalized RF amplitudes at the top of the LVZ. (g-i) Topography of the Moho obtained from CCP stacks. (j-l) Normalized RF amplitudes at Moho. N denotes number of piercing points at each bin. Each column shows results from bins with more than 20, 30 and 40 piercing points.

**Figure S10.** CCP images along eight profiles: (a) AA', (b) BB', (c) CC', (d) DD', (e) EE', (f) FF', (g) GG' and (h) HH'. The locations of the profiles are shown in (i). The RFs are migrated using ak135 global 1-D velocity model (Kennett *et al.* 1995). Symbols in this figure are the same as those in Fig. 6.

**Figure S11.** Variation in discontinuity depths and amplitudes of CCP stacks, using ak135 global velocity model (Kennett *et al.* 1995). (a) Topography of the top of the LVZ obtained from CCP stacks. (b) Moho topography obtained from CCP stacks. (c) Normalized amplitudes at the top of the LVZ. (d) Normalized amplitudes at the Moho. Symbol definitions are the same as those in Fig. 7 (and Fig. 2a).

Please note: Oxford University Press are not responsible for the content or functionality of any supporting materials supplied by the authors. Any queries (other than missing material) should be directed to the corresponding author for the paper.